



Full length article

New modified embedded-atom method interatomic potential to understand deformation behavior in VNbTaTiZr refractory high entropy alloy

Mashroor S. Nitol ^{a,*}, Marco J. Echeverria ^a, Khanh Dang ^a, Michael I. Baskes ^{a,b}, Saryu J. Fensin ^a^a Los Alamos National Laboratory, Los Alamos, NM, 87545, USA^b Department of Materials Science & Engineering, University of North Texas, Denton, TX 76203, USA

ARTICLE INFO

Dataset link: <https://www.ctcms.nist.gov/potentials/>

Keywords:

High entropy alloy
Dislocation
BCC
MEAM
Molecular dynamics

ABSTRACT

High Entropy Alloys (HEAs) have attracted much interest over the past 20 years because of their remarkable mechanical properties. Recent works on BCC refractory HEAs have demonstrated high strength even at extreme temperatures with an unusual mix of strength and ductility. They also show excellent strain-hardening behavior. This study focuses on the VNbTaTiZr alloy, which stands out for its favorable qualities including relatively low density, impressive yield strength, and ductility at room temperature. To better understand the atomic behavior and microstructural features inherent to this alloy, a Modified Embedded Atom Method (MEAM) potential is developed, based on first-principles computations. Through accurate modeling of lattice constants, elastic constants, and formation enthalpies, a hybrid Molecular Dynamics/Monte Carlo (MD/MC) simulation of an equimolar VNbTaTiZr refractory HEA was performed to explore the role of local chemical compositions to its mechanical response. The current MEAM potential aligns closely with recent experimental work, validating its effectiveness. Adding Zr to the VNbTaTi alloy induces more lattice distortion, matching recent experimental observations. The potential also predicts that for RHEAs, deformation behavior is dominated by edge dislocations, unlike in pure BCC elements where screw dislocations prevail. Overall, this potential will be useful for unraveling the intricate atomic-level processes that give this alloy its remarkable mechanical performance.

1. Introduction

Since the emergence of high entropy alloys (HEAs), extensive research has been conducted to explore the origin of their unique mechanical properties, such as exceptional strength at extreme temperatures, a combination of great strength and ductility, and significant strain hardening capabilities. Contrary to conventional alloys, which typically contain one or two major elements, HEAs are characterized by their composition of at least five near-equimolar major elements, spanning a range of 5 to 35 atomic percent. This distinctive composition leads to the manifestation of four core effects: high entropy, lattice distortion, sluggish diffusion, and cocktail effects [1–3]. Among these effects, the high entropy effect stands out as a key factor that enhances the formation of dilute solid solution phases compared to conventional alloys [4]. Additionally, the lattice distortion effect, caused by significant differences in atomic radii, induces substantial strengthening by forming misfit volumes around each atom. These effects are particularly pronounced in body-centered cubic (BCC) HEAs, where the eight nearest neighbors of each atom allow for a higher probability of distinct elements being present in the vicinity, leading to larger lattice distortions [5].

Refractory HEAs (RHEAs) have drawn particular attention due to their remarkable strength above 800 °C. In contrast, widely used Ni alloys lose over 80% of their yield strength around 1000 °C by virtue of thermal softening at these elevated temperatures [6]. In contrast, RHEAs have higher melting temperatures of ~1800 °C, resulting in slower diffusion and better high-temperature strength, making them promising for applications at extreme temperatures. Among the various RHEAs, the VNbTaTiZr alloy has emerged as a particularly intriguing material due to its desirable properties. Notably, it exhibits relatively low density, excellent yield strength (≥ 1300 MPa), and good ductility ($\geq 15\%$) at room temperature. The exceptional mechanical performance of VNbTaTiZr is primarily attributed to lattice distortion as the dominant strengthening mechanism [7,8]. Consequently, investigating the atomistic behavior and microstructural characteristics of this alloy is crucial for a comprehensive understanding of its mechanical properties and potential optimization.

Recent experimental data across a wide range of areas suggests that further in-depth investigation into strengthening and corrosion mechanisms in materials could yield important insights. Specifically, additional gains may be possible in performance and properties with a more

* Corresponding author.

E-mail address: mash@lanl.gov (M.S. Nitol).

thorough understanding, at the atomic level, of the fundamental underpinnings. To enable analysis at this resolution, atomistic simulation has become a powerful approach for probing the intricate structural, kinetic, thermodynamic and mechanical phenomena that govern complex behavior in metals and alloys. Of the available techniques, first principles density functional theory (DFT) calculations currently provide the most accurate means to model and predict fundamental materials properties. However, the practical time and length scales that can be simulated using DFT are limited, typically to simulations on the order of a few nanoseconds and thousands of atoms, which poses challenges for modeling complex plastic deformation phenomena and related defect and dislocation interactions observed experimentally in metals. An alternative is applying semi-empirical interatomic potentials, where interactions are represented by parameterized mathematical functions fit to reproduce target behavior. The accuracy depends greatly on selecting appropriate functions and having reliable parameters to capture all relevant interactions for the alloy systems of interest. In this regard, the modified embedded atom method (MEAM) [9] provides an ideal framework for highly configurable alloys like HEAs, with consistent formalism across many elements and structures [10–13]. However, MEAM potentials have not previously been fully developed for the HEA considered here, VNbTaTiZr, limiting atomistic simulations. Previous efforts to develop interatomic potentials for related refractory high entropy alloys have focused on fitting parameters based on randomly generated solid solution structures of ternary systems [14, 15]. However, extrapolating these simpler three element models to describe more complex four or five element alloys has proven difficult, often failing to accurately reproduce key properties like elastic constants and stacking fault energies. Here, this work puts forward newly parameterized MEAM potential for VNbTaTiZr, specifically targeting fundamental properties like formation enthalpies, lattice parameters, and elastic constants at the alloy level. Moreover, free surface energies and stacking fault energies were fitted to DFT references, enabling accurate representation of lattice distortions, deformation twinning, and other mechanisms seen experimentally. Larger-scale, longer-time dynamics simulations can now explore defect formation, dislocation behavior, phase transformations, and overall mechanical responses. This new MEAM potential lays the groundwork for revealing new atomistic mechanisms underlying the remarkable properties of VNbTaTiZr and related alloys.

2. Methodology: Second nearest neighbor MEAM (2NN MEAM)

MEAM is an excellent many-body potential model, characterized by its high accuracy and reasonable computational efficiency, which has been used extensively in materials modeling for the last few decades. Therefore, MEAM is chosen to characterize the quinary VNbTaTiZr system in this investigation. The fundamental paper by Lee et al. [16] provides a complete formulation and specifics of the MEAM model.

Similar to other interatomic potentials, the MEAM parameters are often fitted to experimental data or first principle calculations of physical, chemical, and mechanical properties of interested material systems. This calibration process is similar to the process followed by other conventional potentials. However, in the case of multi-component systems, it is necessary to take into account the various interactions that span from unary to ternary. In this work, the unary terms were taken from previously published work [9,17,18]. There are fourteen parameters that need to be calibrated to define the binary cross-terms. As an example, for a given A–B elemental pair, these parameters are the cohesive energy (E_c), first nearest-neighbor distance (r_e), exponential decay factor of the universal energy (α), attractive and repulsive terms (d_{att} and d_{rep}), and four sets of screening parameters C_{min} and C_{max} (A–A-B, B–B-A, A–B-A, and A–B-B). Additionally, six parameters associated with C_{min} and C_{max} are needed for defining the ternary cross-terms. For instance, the parameters for the A–B–C elemental combination consist of three sets of minimum and maximum values for C (A–B–C, A–C–B, and

B–C–A). The MEAM formalism has no additional parameters for systems with more than 3 components.

The parameters for the binary and ternary fits were optimized in this study using the *differential evolution* method [19], a stochastic optimization methodology. Differential evolution is able to explore huge regions of the parameter space since it does not rely on gradients to find the minimum. However, a larger number of function evaluations is typically required. Rather than being determined all at once, these values go through a series of steps. Since it is necessary to know all possible parameters for the binary cross-terms before establishing the ternary cross-terms, the ternary cross-term parameters are determined after the binary cross-term parameters have been established. Each possible parameter for a binary or ternary cross-term undergoes a simultaneous determination process.

To understand these cross-terms better, first, it is essential to identify the target attributes associated with the relevant structures. This is key to determining the potential parameters governing these cross-terms. When acquiring properties specific to a cross-term, three important factors must be scrutinized. In this work, the binary alloys ($M–X$) with the formulae $M_{0.75}X_{0.25}$, $M_{0.5}X_{0.5}$, and $M_{0.25}X_{0.75}$ were selected because of high solute concentration. The $M_{0.5}X_{0.5}$ binary alloy was modeled using the $B2$ structure with the $Pm\bar{3}m$ space group, with the M atoms located in the corners of the cuboid and the X atoms in the body center. $a_1 = (a, 0, 0)$, $a_2 = (0, a, 0)$, and $a_3 = (0, 0, a)$ were the primordial Bravais lattice vectors. The $M_{0.75}X_{0.25}$ and $M_{0.25}X_{0.75}$ binary alloys were modeled using the DO_3 structure in the $Fm\bar{3}m$ space group. The basic Bravais lattice vectors were provided as $a_1 = (0, a, a)$, $a_2 = (a, 0, a)$, and $a_3 = (a, a, 0)$, where a denotes the lattice constant of a typical BCC unit cell. The simulation cell consists of eight conventional BCC unit cells. For $M_{0.25}X_{0.75}$, the atomic locations were $4a(0, 0, 0)$ for M atom, $4b(0.5, 0.5, 0.5)$ site for first X ($X[I]$) atom, and two X atoms ($X[II]$) site were in the $8c(0.25, 0.25, 0.25)$ position. Furthermore, the phase diagrams of Ti–X and Zr–X binary alloys have already been investigated [20,21], revealing that (a) the Ti–X ($X=V, Nb, Ta$) binary alloy exhibits a stable HCP phase near the pure Ti region at $T = 0$ K, (b) a BCC phase becomes stabilized with an increasing amount of the X element, and (c) ultimately, a BCC single phase attains stability when the X element reaches a sufficient quantity. There may be more metastable phases in these alloys that can be altered via heat treatment, such as alpha prime (α') or omega (ω) phases, but for the time being it is assumed that these binary alloys only adhere to the single BCC phase described above. Characterizing the $B2$ structures for binary alloys takes precedence over studying random solid solutions because of having single BCC phase of this HEA alloy. Additionally, the enthalpies of the DO_3 structure are fitted to ensure completeness and while doing so considered both the binary combinations of AB_3 and A_3B in DO_3 structures.

Second, it is important to select certain characteristics for these structures. Since the mechanical deformation and failure mechanism of the RHEA is of interest in this work, three physical properties are calculated using DFT for all relevant structures: formation enthalpy, lattice constant, and elastic constants at 0 K. The goal is to determine how well these elements can be combined, and whether the parameters used for the cross-terms are appropriate. Such values can be obtained by either first-principles calculations or experimental data. Due to the paucity of experimental data for many of the structures considered here, first-principles calculations based on DFT were employed to determine the necessary values. Here, the $Fmm2$ structure received particular emphasis since the structure adopts a BCC motif, where each atom has eight nearest neighbors at a distance known as the first nearest neighbor distance. The $Fmm2$ structure is an orthorhombic crystal structure. In this structure, the first nearest neighbor elements alternate with each other. The first nearest neighbors are atoms of different species, while atoms of the same species are found in the second nearest neighbor positions. In the $Fmm2$ structure, which is composed of $A4B4C4$ units, the combinations of ABC can be VNbTa,

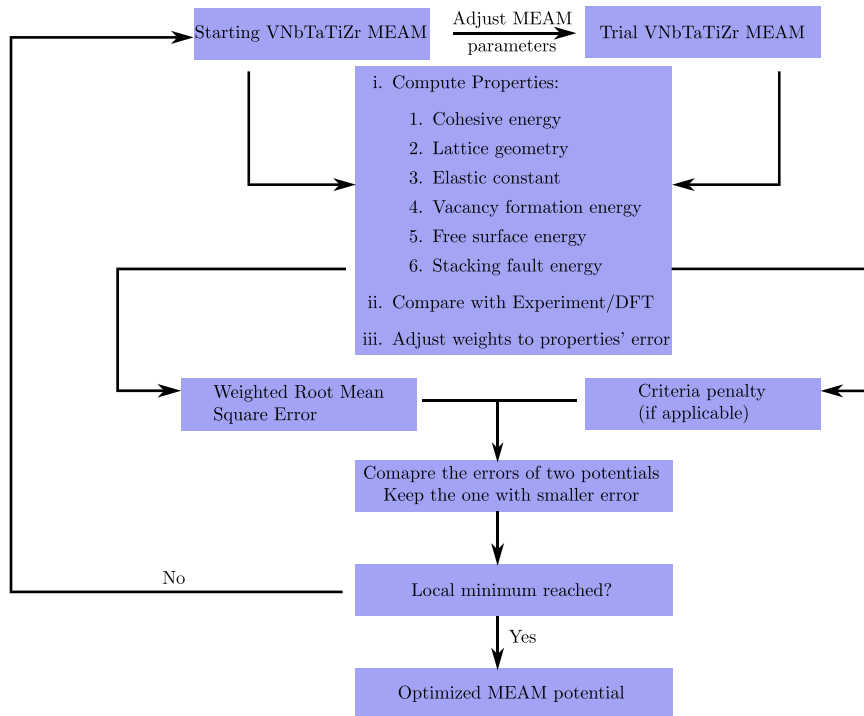


Fig. 1. The parameter optimization algorithm employed for the development of the HEA MEAM potential in the current study.

VNbTi, VNbZr, NbTaTi, NbTiZr, or TaTiZr. The positions of these units within the orthorhombic unit cell are defined as follows: A: (0,0,2/3; 0,1/2,1/6; 0.5,0,1/6; 1/2, 1/2, 2/3); B: (0,0,0; 0,0.5,0.5; 0.5,0,0.5; 0.5,0.5,0.0); C: (0.5,0,0.33/40; 0.5,0.5,13/40; 0,0.13/40; 0,0.5,33/40). The orthorhombic unit cell is determined by its lattice vectors: $a_1 = (a, 0, 0)$; $a_2 = (0, 2a, 0)$; $a_3 = (0, 0, 4.11a)$. The ultimate MEAM values derived for the binary combinations, denoted as $A - B$, have been documented in Table 1. Regarding the ternary potentials, the calibration process revolves around six screening parameters pertaining to all three atoms, and these values have been recorded in Table 1 as well. The nomenclature used to denote the screening parameters, specifically C_{A-B-C}^{\max} and C_{A-B-C}^{\min} , aligns with the conventions established by LAMMPS [22], where the notation $A - B - C$ signifies that atom C is screening atoms A and B . The parameter optimization process is schematically shown in Fig. 1.

The VASP code [23,24] was utilized for conducting the DFT calculations. The Perdew–Burke–Ernzerhof generalized gradient approximation (GGA) [25] was employed for the exchange–correlation functional, along with the projector-augmented wave (PAW) method [26]. For the plane-wave basis set, a cutoff energy of 520 eV was applied, and the Methfessel–Paxton smearing method with a width of 0.1 eV was utilized. In the case of $B2$ structures, a k -point mesh of $19 \times 19 \times 19$ was chosen, while the corresponding k -point density was used for other binary and ternary structures. To determine the equilibrium lattice constant and bulk modulus, the Birch–Murnaghan equation of state was employed, fitting it to a volume range spanning from $0.9V_0$ to $1.1V_0$ (where V_0 represents the equilibrium volume). Elastic constants were calculated by subjecting a cell in the equilibrium structure to strains ranging from -5% to $+5\%$. Throughout the calculations, atomic positions were relaxed, with convergence criteria set to 10^{-10} eV for energy and 10^{-4} eV/A for forces.

3. Results

3.1. Molecular statics (MS)

3.1.1. Elastic properties of binary and ternary structures to fit MEAM potential

Table 2 presents the computed elastic constants, formation energies, and lattice parameters for $B2$ structures, obtained through DFT and the current MEAM potential. Additionally, prior MEAM potentials for analogous binary alloys are documented. It is worth noting that, due to both Ti and Zr having the '*HCP*' configuration as a reference state, there were issues with reproducing the $B2$ elastic constant. An effort was made to adopt '*BCC*' as a reference state for Ti and Zr, as per the work of Maisel et al. [17]. However, it was subsequently discovered that the inclusion of V as a dilute alloying element in a Ti matrix in previous MEAM potential Maisel et al. [17] rendered the potential unstable leading to a negative stacking-fault energy. The calculated elastic constants, C_{11} and C_{12} , for the binary combinations were only 5% or less off from the DFT values. However, it is important to note that the value for C_{44} did not match these calculations well. The new MEAM potential developed in this work shows much better agreement with DFT calculations compared to previous MEAM potentials [14,15], especially for elastic constants. The current MEAM potential has an RMSE of 11.34 versus DFT, while the previous MEAM potential had an RMSE of 111.09 for V-Nb, V-Ti, and V-Zr binaries, and an RMSE of 37.63 for Nb-Ta, Nb-Ti, Nb-Zr, Ta-Ti, Ta-Zr, Ti-Zr binaries, respectively. For formation enthalpies, both the new and old MEAM potentials have similar, low RMSE values around 0.02. For lattice constants, the RMSE is 0.01 for the new potential. While the new and old MEAM potentials have comparable accuracy for formation enthalpies and lattice constants, the current MEAM potential reproduces the elastic constants better. This indicates that the current MEAM potential will be more appropriate to use when investigating mechanical properties of the VNbTaTiZr systems.

Table 1

2NN MEAM potential parameter sets for the pure, binary, and ternary combinations of V, Nb, Ta, Ti, and Zr. All parameters are dimensionless other than the cohesive energy, E_c (eV/atom), the equilibrium nearest-neighbor distance, r_e (Å), and the bulk modulus, B (GPa).

Unary potentials														
E_c	r_e	B	A	$\beta^{(0)}$	$\beta^{(1)}$	$\beta^{(2)}$	$\beta^{(3)}$	$t^{(1)}$	$t^{(2)}$	$t^{(3)}$	C_{min}	C_{max}	d	
V [17]	5.30	2.60	158.62	0.46	5.11	4.27	0.04	0.45	1.23	-4.01	-4.97	0.49	2.25	0.00
Nb [9]	7.47	2.86	173.00	0.72	5.08	1.00	2.50	1.00	1.70	2.80	-1.60	0.36	2.80	0.00
Ta [9]	8.09	2.86	194.00	0.67	4.49	1.00	1.00	1.00	1.70	2.10	-3.20	0.25	2.80	0.00
Ti [18]	4.87	2.92	110.00	0.66	2.70	1.00	3.00	1.00	6.80	-2.00	-12.00	1.00	1.44	0.00
Zr [18]	6.36	3.20	97.00	0.68	2.45	1.00	3.00	2.00	6.30	-3.30	-10.00	1.00	1.44	0.00
Binary potentials														
Ref	E_c	r_e	α	d_{att}	d_{rep}	C_{ABA}^{min}	C_{ABB}^{min}	C_{BBA}^{min}	C_{AAB}^{min}	C_{ABA}^{max}	C_{ABB}^{max}	C_{BBA}^{max}	C_{AAB}^{max}	
VNb	B2	6.53	2.75	4.75	0.00	0.00	0.47	0.77	0.89	0.15	2.05	2.23	2.13	0.73
VTa	B2	7.79	2.74	4.49	0.00	0.00	0.76	0.14	0.75	0.53	2.05	2.71	1.51	2.53
VTi	B2	5.68	2.70	4.39	0.00	0.00	0.43	0.25	0.86	0.54	2.18	2.10	2.10	1.75
VZr	B2	5.93	2.86	4.48	0.00	0.00	0.26	0.75	0.56	0.20	2.65	2.33	1.66	0.73
NbTa	B2	7.79	2.87	4.93	0.00	0.00	0.50	0.33	0.84	0.21	1.82	2.66	2.32	1.50
NbTi	B2	6.13	2.83	4.46	0.00	0.00	0.38	0.41	0.22	0.22	1.59	1.55	1.92	0.75
NbZr	B2	6.81	2.97	4.37	0.00	0.00	0.57	0.55	0.54	0.20	1.66	1.66	1.79	0.78
TaTi	B2	6.62	2.83	4.58	0.00	0.00	0.47	0.37	0.42	0.27	2.15	2.24	1.71	0.88
TaZr	B2	6.41	2.98	4.67	0.00	0.00	0.38	0.88	0.78	0.23	2.09	1.53	1.65	0.88
TiZr	B2	5.58	2.96	4.39	0.00	0.00	0.52	0.34	0.75	0.45	2.12	2.14	1.81	1.77
Ternary potentials														
				C_{ABC}^{min}	C_{ACB}^{min}	C_{BCA}^{min}	C_{ABC}^{max}	C_{ACB}^{max}	C_{BCA}^{max}					
				VNbTa	0.49	0.39	0.72	2.15	1.01	1.29				
				VNbTi	0.81	0.41	0.39	2.28	1.73	1.84				
				VNbZr	0.25	0.32	0.35	2.37	1.11	0.86				
				VTaTi	0.50	0.95	1.03	1.11	2.10	2.78				
				VTaZr	0.17	0.31	0.29	2.25	2.75	2.20				
				VTiZr	0.29	0.44	0.54	2.62	1.96	1.44				
				NbTaTi	0.64	0.78	0.40	1.51	1.31	2.65				
				NbTaZr	0.55	0.27	0.12	2.30	1.44	1.49				
				NbTiZr	0.41	0.38	0.98	1.22	1.22	1.93				
				TaTiZr	0.48	0.34	0.20	1.86	1.29	1.22				

Table 2

Comparison of lattice constants (Å), elastic constants (GPa), and formation enthalpies (ΔH , eV/atom) at 0 K for binary alloys. The results obtained from both present and previous DFT calculations and MD simulations using the developed potential in this work are compared. Furthermore, a comparison is made with previous MEAM potentials for RHEA alloys.

Structure	composition	Method	$a = b = c$	$B = (C_{11} + 2C_{12})/3$	C_{44}	ΔH
	V-Nb	DFT	3.17	174.19 [27]	10.72 [27]	-0.19
		MEAM(present)	3.16	168.24	9.41	-0.22
		MEAM [14]	3.17	170.82	94.97	-0.15
	V-Ta	DFT	3.17	189.54	42.98	-1.09
		MEAM(present)	3.17	176.07	73.29	-1.09
	V-Ti	DFT	3.12	138.07 [27]	33.6 [27]	0.12
		MEAM(present)	3.12	128.31	62.87	0.12
		MEAM [14,17]	3.19,3.08	137.74,118.29	146.84,285.16	0.08,0.05
	V-Zr	DFT	3.30	119.36	15.38	-0.22
		MEAM(present)	3.29	121.66	20.52	-0.28
		MEAM [14]	3.24	129.64	70.07	-0.27
	Nb-Ta	DFT	3.32	187.16	48.80	-0.004
B2		MEAM(present)	3.32	185.35	51.22	-0.02
		MEAM [15]	3.32	196.39	61.64	-0.00
	Nb-Ti	DFT	3.27	134.93 [27]	12.8 [27]	0.03
		MEAM(present)	3.26	126.88	28.97	0.03
		MEAM [15,28]	3.26,3.31	144.29,22.83	81.57,27.81	0.03,0.34
	Nb-Zr	DFT	3.43	120.33 [27]	18.3 [27]	0.10
		MEAM(present)	3.43	116.15	34.86	0.10
		MEAM [15]	3.43	126.53	78.03	0.10
	Ta-Ti	DFT	3.27	143.21 [27]	39 [27]	0.06
		MEAM(present)	3.27	138.64	53.38	0.06
		MEAM [15]	3.26	150.24	106.47	0.06
	Ta-Zr	DFT	3.44	133.22	38.19	0.17
		MEAM(present)	3.43	123.92	53.85	0.17
		MEAM [15]	3.44	134.45	94.60	0.17
	Ti-Zr	DFT	3.42	95.03 [29]	36.60 [29]	0.02
		MEAM(present)	3.42	95.57	59.74	0.02
		MEAM [15]	3.43	94.3	59.75	0.02

Table 3

Comparison of elastic constants (GPa) at 0 K for ternary formed structure (*Fmm2*) used to fit 3-body terms parameter. The results obtained from both present MEAM and DFT calculations are compared.

Structure	Composition	C_{11}	C_{12}	C_{13}	C_{22}	C_{23}	C_{33}	C_{44}	C_{55}
<i>Fmm2</i>	VNbTa	DFT MEAM	258.00 247.72	131.78 136.01	154.99 173.09	256.30 247.10	163.21 136.12	215.32 221.51	41.86 44.34
	VNbTi	DFT MEAM	206.28 192.75	115.47 109.84	115.97 124.64	188.36 206.17	138.95 96.41	189.57 197.63	32.97 36.07
	VNbZr	DFT MEAM	162.63 165.78	107.33 93.58	119.58 125.00	156.66 192.83	107.14 85.22	167.93 166.85	22.62 28.32
	VTaTi	DFT MEAM	204.98 200.33	133.57 129.59	126.61 115.13	204.12 222.29	123.82 95.64	206.54 231.53	39.19 43.79
	VTaZr	DFT MEAM	176.34 180.02	109.79 104.29	119.03 124.04	181.67 225.74	106.35 81.40	182.45 196.06	36.83 38.14
	VTiZr	DFT MEAM	114.36 181.39	87.76 61.36	84.51 95.11	158.70 181.38	88.87 95.10	145.99 134.75	47.90 63.44
	NbTaTi	DFT MEAM	207.45 192.80	126.76 125.11	131.96 131.47	214.28 222.23	131.67 96.20	198.73 199.50	28.88 24.11
	NbTaZr	DFT MEAM	194.53 183.31	113.22 111.14	111.97 114.57	180.12 206.91	111.14 83.08	201.69 191.04	27.93 17.64
	NbTiZr	DFT MEAM	207.45 155.20	126.76 94.73	131.96 85.62	214.28 182.18	131.67 58.87	198.73 166.17	17.88 13.20
	TaTiZr	DFT MEAM	207.45 168.03	126.76 101.88	131.96 92.55	214.28 208.25	131.67 51.93	198.73 183.62	20.88 14.56

Table 3 displays the elastic constants of the ternary compositions via DFT and MD simulations using this MEAM potential. As previously stated, the target structure for the three-body terms is the *Fmm2* orthorhombic configuration, characterized by eight independent elastic constants. The MEAM potential reproduces all elastic constants with less than a 10% margin of error for any ternary combinations. It is imperative to mention that, in addition to elastic constants, the potential is also fitted with target parameters such as stacking fault energies, vacancy formation energies, and free surface energies of binary alloys. Given that the MEAM potential formulation does not permit the fitting of four-body or five-body term combinations, it is critical to match all these the two- and three-body target parameters within with the database, there exists a reasonable likelihood of obtaining higher-order properties that approximate DFT or experimental behavior.

3.1.2. Elastic properties of special quasi-random structures

To determine if the model can capture the random solid solutions found in RHEAs, special quasi-random structures (SQS) [30] were constructed using the Alloy Theoretic Automated Toolkit (ATAT) [31] tool. SQS mimics the randomness of real alloys while using a periodic supercell. SQS models were built for the VNbTaTiZr 5-element RHEA and its 3- and 4-element subsystems. For the DFT calculations, BCC supercells were generated with dimensions of $3 \times 3 \times 3$ (54 atoms), $4 \times 4 \times 4$ (128 atoms), and $5 \times 5 \times 5$ (250 atoms) unit cells for the 3-, 4-, and 5-element alloys, respectively. The Brillouin zone was sampled at a resolution of $2\pi \times 0.03 \text{ \AA}^{-1}$. Other DFT parameters such as cut-off energy and k -points mesh were taken similar to those stated previously. For the MD simulations, the present MEAM potential and two from previous studies [14,15] were tested for the RHEA compositions. For both DFT and MD simulations, the effective BCC elastic constants were extracted from the calculated stiffness matrices [32]:

$$C_{11}^\dagger = \frac{C_{11} + C_{22} + C_{33}}{3} \quad (3.1)$$

$$C_{12}^\dagger = \frac{C_{12} + C_{13} + C_{23}}{3} \quad (3.2)$$

$$C_{44}^\dagger = \frac{C_{44} + C_{55} + C_{66}}{3} \quad (3.3)$$

In addition, the equivalent isotropic elastic constants were calculated using the Hill averaging method [33]. The Hill averaging technique provides bulk modulus values that closely match experimental measurements. The elastic constants also determined the Zener

anisotropy ratio (A_c). This ratio measures how much the elastic properties of the alloys differ along different crystal directions. A perfectly isotropic material would have $A_c = 1$, while values greater than 1 indicate increased anisotropy or directional dependence. To quantify the overall elastic isotropy, the isotropic Poisson's ratio ν^H , isotropic shear modulus μ^H , and isotropic Young's modulus E_Y^H were also determined. These effective isotropic constants represent the polycrystalline aggregate behavior averaged over all crystal orientations. The equations for calculating these average elastic moduli from the single crystal constants are given in Eqs. (3.4)–(3.7) and **Table 4** summarizes the calculated results for these parameters.

$$\nu^H = \frac{C_{11}^\dagger + 4C_{12}^\dagger - 2C_{44}^\dagger}{8C_{11}^\dagger + 12C_{12}^\dagger + 4C_{44}^\dagger} + \frac{\left(C_{11}^\dagger\right)^2 + 2C_{12}^\dagger \left(3C_{44}^\dagger - C_{12}^\dagger\right) + C_{11}^\dagger \left(C_{12}^\dagger - 2C_{44}^\dagger\right)}{4 \left[\left(C_{11}^\dagger\right)^2 + C_{12}^\dagger \left(C_{44}^\dagger - 2C_{12}^\dagger\right) + C_{11}^\dagger \left(C_{12}^\dagger + 3C_{44}^\dagger\right)\right]} \quad (3.4)$$

$$\mu^H = \frac{C_{11}^\dagger + 3C_{44}^\dagger - C_{12}^\dagger}{10} + \frac{5 \left(C_{11}^\dagger - C_{12}^\dagger\right) C_{44}^\dagger}{6C_{11}^\dagger - 6C_{12}^\dagger + 8C_{44}^\dagger} \quad (3.5)$$

$$E_Y^H = 2\mu^H(1 + \nu^H) \quad (3.6)$$

$$A_c = 2C_{44}^\dagger / (C_{11}^\dagger - C_{12}^\dagger) \quad (3.7)$$

As shown in **Table 4**, the newly developed MEAM potential shows significant improvement of the previous HEA potentials, with an RMSE of just 12.38 across all calculated properties compared to 48.46 for earlier MEAM potentials for VNbTiZr [14] and NbTaTiZr [15]. This improved accuracy stems from the fact that the current MEAM potential is trained on a broader range of DFT data, rather than just lattice constants and formation energies like before. While the previous RHEA potentials incorrectly predict near-isotropic structures for NbTiZr, NaTaTi, and NbTaZr, the new MEAM correctly captures the high anisotropy in agreement with DFT. Even at elevated temperatures, the MEAM potential closely captures the elastic stiffness tensor for the VNbTaTi alloy, especially the complex interplay between four- and five-body force combinations in agreement with DFT. Overall, the accuracy of the multiple properties for 2- and 3-combinations of the HEA elements gives confidence that the new VNbTaTiZr potential accurately captures the alloy's elastic behavior.

Table 4

Key properties calculated for the VNbTaTiZr high entropy alloy and its 3-element and 4-element subsystems using DFT and the present MEAM potential. These include: Lattice parameter a_0 (in Å), Cohesive energy E_{coh} (in eV), effective elastic constants C_{11}^\dagger , C_{12}^\dagger , and C_{44}^\dagger (in GPa), Zener anisotropy ratio A_c , isotropic Poisson's ratio ν^H , isotropic shear modulus μ^H (in GPa), isotropic Young's modulus E_Y^H (in GPa), shear modulus ($C' = (C_{11}^\dagger - C_{12}^\dagger)/2$), bulk modulus ($B = (C_{11}^\dagger + 2C_{12}^\dagger)/3$). To ensure consistency, each alloy composition's properties are averaged across 5 SQS structures. Results from the previous MEAM potential for similar alloy compositions are also provided for comparison.

	a	E_{coh}	C_{11}^\dagger	C_{12}^\dagger	C_{44}^\dagger	A_c	ν^H	μ^H	E_Y^H	C'	B
VNbTa (DFT [34])	3.22		239.00	130.00	40.00	0.73	0.38	45.28	124.54	54.50	166.33
VNbTa (present MEAM)	3.22	7.47	233.07	150.71	46.24	1.12	0.39	44.14	122.33	41.18	178.16
VNbTi (DFT [35])	3.20		184.30	126.10	39.90	1.37	0.39	35.16	97.62	29.10	145.50
VNbTi (present MEAM)	3.19	6.13	182.13	117.03	50.63	1.56	0.36	42.41	115.47	32.55	138.73
VNbTi (MEAM [14])	3.19	6.13	171.51	68.95	58.54	1.14	0.27	55.52	141.21	51.28	103.14
VNbZr (DFT)	3.31		162.01	101.21	49.72	1.64	0.35	40.82	110.12	30.40	121.48
VNbZr(presentMEAM)	3.30	6.40	168.61	104.76	47.39	1.48	0.36	40.45	109.63	31.93	126.04
VNbZr(MEAM [14])	3.33	6.26	158.26	72.59	54.49	1.27	0.29	49.48	127.64	42.84	101.15
VTaTi (DFT)			197.22	105.92	69.31	1.52	0.31	58.63	153.83	45.65	136.35
VTaTi(presentMEAM)	3.19	6.68	210.60	117.29	73.53	1.58	0.32	61.27	161.58	46.65	148.40
VTaZr (DFT)	3.29		172.11	103.21	52.48	1.52	0.34	44.33	119.05	34.45	126.18
VTaZr(presentMEAM)	3.30	6.67	187.32	107.68	68.12	1.71	0.32	54.92	144.99	39.82	134.23
VTiZr (DFT)	3.28		152.87	87.24	56.61	1.73	0.32	45.49	119.81	32.82	109.12
VTiZr(presentMEAM)	3.29	5.70	150.23	90.87	64.55	2.17	0.31	47.26	124.11	29.68	110.66
VTiZr(MEAM [14])	3.30	5.42	129.86	67.22	46.76	1.49	0.30	39.82	103.82	31.32	88.10
NbTiZr (DFT [36])	3.39		143.00	111.00	64.00	4.00	0.36	36.95	100.69	16.00	121.67
NbTiZr (present)	3.39	6.10	134.40	95.14	50.36	2.57	0.36	34.52	93.62	19.63	108.23
NbTiZr (MEAM [14])	3.42	6.20	153.78	65.29	65.13	1.47	0.25	55.78	139.90	44.24	94.79
NbTaTi (DFT)	3.29		167.04	121.21	43.21	1.89	0.39	33.50	92.90	22.92	136.49
NbTaTi(presentMEAM)	3.29	6.73	177.02	130.00	51.55	2.19	0.38	37.62	103.91	23.51	145.67
NbTaTi(MEAM [15])	3.33	6.26	247.76	107.74	86.22	1.23	0.28	79.33	203.18	70.01	154.42
NbTaZr (DFT)	3.41		157.43	112.65	44.08	1.97	0.38	33.59	92.63	22.39	127.58
NbTaZr(presentMEAM)	3.41	6.90	160.98	117.87	53.14	2.47	0.37	37.01	101.55	21.55	132.24
NbTaZr(MEAM [15])	3.43	7.24	225.75	69.81	77.10	0.99	0.24	77.45	191.70	77.97	121.79
TaTiZr (DFT)	3.38		127.89	91.22	44.21	2.41	0.36	31.06	84.71	18.34	103.44
TaTiZr(presentMEAM)	3.39	6.04	136.99	104.10	64.64	3.93	0.35	37.56	101.66	16.44	115.06
TaTiZr(MEAM [15])	3.39	6.36	170.46	90.05	80.74	2.01	0.28	61.03	155.95	40.20	116.85
VNbTaTi (DFT) [37]	3.22		211.80	131.20	31.60	0.78	0.40	34.83	97.35	40.30	158.07
VNbTaTi (present MEAM)	3.22	6.78	194.50	129.88	43.99	1.36	0.38	38.88	107.43	32.31	151.42
VNbTaTi (Expt,300K [37])			196.80	121.40	46.70	1.24	0.37	42.86	117.17	37.70	146.53
VNbTaTi (present MEAM)	3.27		188.92	130.68	51.37	1.76	0.38	40.91	112.50	29.12	150.09
VNbTaTi (Expt,773K [37])			190.50	129.90	46.00	1.52	0.38	38.91	107.45	30.30	150.10
VNbTaTi (present MEAM)	3.31		179.23	132.22	48.79	2.08	0.39	36.39	100.91	23.51	147.89
VNbTaTi (Expt,973K [37])			184.30	122.50	45.90	1.49	0.37	39.17	107.68	30.90	143.10
VNbTaTi (present MEAM)	3.34		173.68	131.99	45.47	2.18	0.39	33.25	92.71	20.85	145.89
VNbTaZr (DFT)	3.22		201.18	123.92	48.61	1.26	0.37	44.34	121.06	38.63	149.67
VNbTaZr (present MEAM)	3.24	6.87	182.61	118.64	53.48	1.67	0.36	43.51	118.28	31.98	139.96
VNbTiZr (DFT [38])			166.40	94.70	53.80	1.50	0.33	45.72	121.55	35.85	118.60
VNbTiZr (present MEAM)	3.29	6.08	156.77	99.85	53.48	1.88	0.34	41.52	111.57	28.46	118.82
VNbTiZr(MEAM [14])	3.31	5.87	141.99	62.29	54.87	1.38	0.27	48.27	122.61	39.85	88.85
VTaTiZr (DFT)	3.28		156.72	97.62	63.41	2.15	0.32	46.67	123.63	29.55	117.32
VTaTiZr(present MEAM)	3.29	6.28	169.05	103.43	68.08	2.07	0.32	50.79	134.24	32.81	125.30
NbTaTiZr (DFT [39])	3.38		172.40	100.70	55.10	1.54	0.33	46.38	123.78	35.85	124.60
NbTaTiZr (present MEAM)	3.37	6.40	149.62	109.21	55.14	2.73	0.36	36.88	100.57	20.20	122.68
NbTaTiZr (MEAM [15])	3.38	6.63	197.64	80.51	78.53	1.34	0.26	69.82	175.34	58.56	119.56
VNbTaTiZr (DFT)	3.28		170.54	106.78	54.48	1.71	0.35	43.94	118.29	31.88	128.03
VNbTaTiZr (present MEAM)	3.29	6.48	166.77	111.86	56.53	2.06	0.35	42.31	114.51	27.45	130.16

3.1.3. Generalized stacking fault energy

Stacking faults play a critical role in determining the deformation mechanisms in crystalline materials. As planar defects are generated by dislocation glide, the stacking fault energy determines the ease of dislocation nucleation and motion [40]. Therefore, quantifying stacking fault energies provides key insights into slip systems, work hardening behavior, and overall strength in metals and alloys [41]. Here, the effects of different alloying elements on the unstable stacking fault energy (γ_{USFE}) of a VNbTaTiZr high entropy alloy were investigated through calculations of generalized stacking fault energy (GSFE) curves. Using DFT and MS calculations, the primary focus was to understand how introducing different elements influences the unstable stacking behavior in these complex solid solutions. To calculate the GSFE, a slip plane within the SQS must first be selected. Each SQS contains multiple slip planes with distinct atomic arrangements, leading to variations in GSFE between planes as shown in Fig. 2(a).

To obtain GSFE curves for each unique plane, the following procedure was undertaken. For demonstration, the description focuses on the $\{110\}$ plane in the VNbTaTiZr alloy, but the same methodology was applied to higher-order planes and all alloy combinations. For both DFT and MS simulations, the BCC unit cell orientation was set along $x \parallel [111]$, $y \parallel [\bar{1}\bar{1}2]$, $z \parallel [1\bar{1}0]$ directions, and then replicated $1 \times 1 \times 12$ times, yielding a total of 72 atoms for 3-element and 4-element alloys. In the 3-element SQS, each atom type was represented by 24 atoms, while the 4-element version featured 18 atoms per type. In the case of the 5-element alloy, the SQS structure was replicated $1 \times 1 \times 15$ times, resulting in 90 atoms, with 18 atoms per type. To prevent interactions between periodic images, a 10 Å vacuum space was introduced along the z -direction. The procedure to create stacking faults in the $\{112\}$ plane followed a similar approach, with orientation changes: $x \parallel [111]$, $y \parallel [\bar{1}\bar{1}0]$, $z \parallel [\bar{1}\bar{1}2]$. The constructed SQS structures

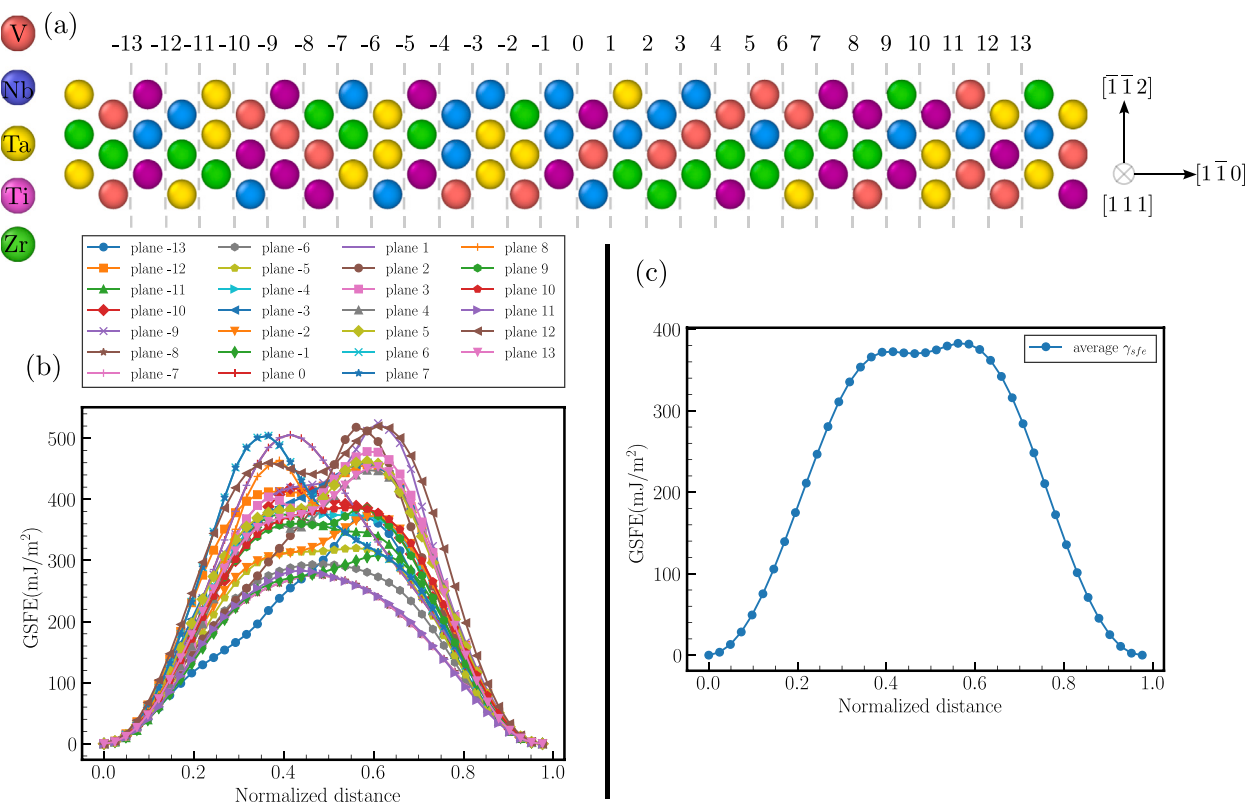


Fig. 2. (a) The distinct chemical composition in each atomic plane of the VNbTaTiZr system. The middle plane is denoted as 0. (b) The calculated GSFE curves for each chemically distinct plane. (c) The average GSFE is obtained by aggregating the data from the individual curves in (b) for $\{111\}[110]$.

were first relaxed using optimization methods. Specifically in DFT simulations, the structures were relaxed until the ionic forces converged within 0.001 eV/atom using the quasi-Newton algorithm and Fermi smearing. For the molecular static simulations, energy minimization was realized using the conjugate gradient algorithm. The relaxation was terminated when either the energy change between successive steps fell below a threshold value (10^{-12}) or the magnitude of the global force vector for all atoms fell below 10^{-12} eV/Å. These initial computational procedures ensured the modeled structures were at an energy minimum before introducing defects.

Stacking faults were introduced by displacing the top atomic planes relative to the bottom planes along the $\{111\}$ direction. While the outermost two top and bottom planes were fixed, the central planes were allowed to relax perpendicular to the shear direction as shown in Fig. 2(a). Displacements were applied up to one lattice periodic length to generate a full stacking fault energy curve. It was found that each distinct atomic plane in the RHEA model exhibited slightly different fault curve behavior based on the chemical composition of that particular plane, as shown in Fig. 2(b). Fig. 2(c) represents the averaged GSFE, derived from the combined data in Fig. 2(b), reflecting variations in local chemical composition within the 3D random solid solution structure. Each fault curve samples a different crystallographic plane with unique atomic arrangements and compositions. The average GSFE curves for both $\{110\}$ and $\{112\}$ planes, calculated using the current MEAM potential, are illustrated in Fig. 3. The effect of chemical composition and atomic arrangement was most noticeable in the unstable stacking fault energies. The calculated average unstable stacking fault energies (γ_{usfe}) are reported in Table 5 for each plane and alloy system. A clear trend emerges across all the DFT and MS results — the $\{110\}$ planes exhibit lower fault energies compared to $\{112\}$. This observation provides valuable insights into slip plane selection in these BCC alloys, as the crystallographic slip mode relates closely to deformation resistance. At its core, these findings highlight the critical

Table 5

Average unstable stacking fault energies (γ_{usfe}) for $\{110\}$ and $\{112\}$ planes from DFT and current MEAM Potential, in mJ/m². The DFT calculations from prior studies are written in *italics*.

Alloy	$\{110\}$		$\{112\}$	
	DFT	MEAM	DFT	MEAM
VNbTa	644,631 [42]	685	816	858
VNbTi	504,491 [42]	508	613	645
VNbZr	720	727	888	892
VTaTi	701	724	804	839
VTaZr	689	696	848	889
VTiZr	583	602	824	857
NbTaTi	569	575	668	702
NbTaZr	626	649	643	668
NbTiZr	457,390 [43]	464	578	601
TaTiZr	518	524	550	578
VNbTaTi	604,560 [42]	617	571	588
VNbTaZr	674	695	744	745
VNbTiZr	474	479	489	505
VTaTiZr	661	663	668	697
NbTaTiZr	476	495	548	553
VNbTaTiZr	359	371	397	407

influence of local chemistry on stacking faults within the complex solid solution alloys. In the nanoscale volume comprising the slip plane and nearby layers, elemental composition fluctuates from the nominal alloy ratios. These atom-to-atom variations allow shear displacement along distinct planes to access slightly higher or lower energy states. Accurately accounting for these local composition effects will be key to predicting dislocation glide and strength in multi-principal element alloys.

3.1.4. Chemical short-range ordering at room temperature

The present MEAM potential was used to investigate short-range chemical ordering in an equimolar RHEA through combined MD/MC

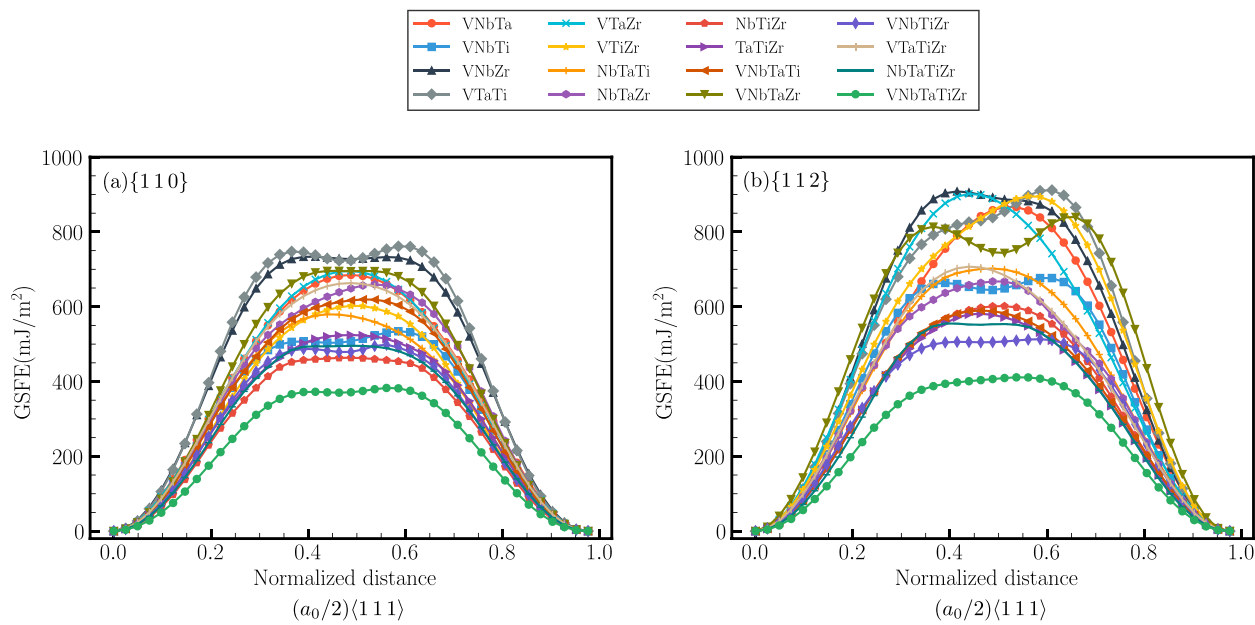


Fig. 3. GSFE of equiatomic VNbTaTiZr and its 3-element and 4-element subsystems for both {110} and {112} planes.

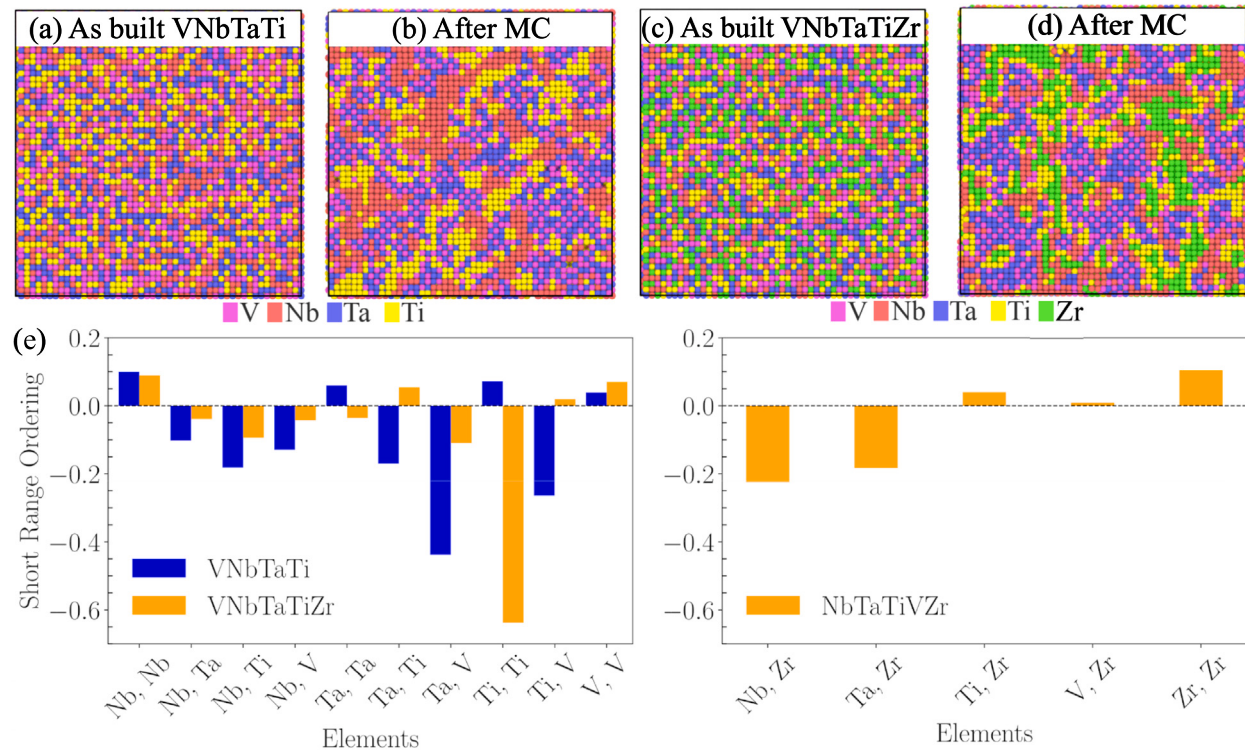


Fig. 4. As built systems and after atom swapping and short-range ordering calculation.

simulations. The MC model optimized the elemental distribution at ambient conditions (300K and zero pressure) using site-occupancy swaps [44] with an isothermal-isobaric ensemble (NPT). The process initiated with a substantial number of attempted swaps ($X = 750$) every N timesteps ($N = 50$) over 130,000 steps, resulting in a total of 1.95 million swaps. This was followed by ten loops with reduced X and N values ($X = 125$, $N = 25$), each running 13,000 steps and 0.65 million swaps. Numerous swaps were performed to ensure that the energy difference between the swaps was less than 0.01 meV. The comparison between as-built structures and those post-MC is illustrated in Fig. 4(a-d).

The Warren-Cowley short-range order (SRO) [45–47] parameter was used to quantify the chemical short-range order (CSRO) in the optimized microstructures shown in Fig. 4. A completely random distribution yields a CSRO of zero. For unlike atom pairs, a negative value indicates an excess of those pairs (e.g. Ta-V), while a positive value signifies a deficit (e.g. Nb-Ta). The reverse is true for like atom pairs - a positive value suggests an excess (e.g. Nb-Nb) [48]. In both VNbTaTi and VNbTaTiZr, the SRO analysis shows Ta and V form a solid solution, while Ti segregates around these elements. Nb forms distinct clusters as a pure element within the solid solution, which is also the case of Zr. Ti clusters separate the Zr and TaV. This segregation

Table 6

Comparison of the average lattice distortions for VNbTaTi and VNbTaTiZr obtained from literature [50] and this work.

	Average lattice distortion, \bar{u}^D (\AA)
VNbTaTi	VNbTaTiZr
Theoretical calculations [50]	0.1443
Synchrotron diffraction [50]	0.1482
Neutron diffraction [50]	0.1450
HR-TEM [50]	0.1380
HAADF-STEM [50]	0.1120
MEAM (present)	0.1384
	0.1777
	0.1781
	0.1783
	0.1779
	0.1610
	0.2310

matches the formation enthalpy trends — the lowest energy structures for each binary show Ta-V, Ti-Zr, and Nb-Nb pairs are energetically favorable [49]. This provides confidence in utilizing the new potential for realistic modeling of intricate chemical configurations in RHEAs.

3.1.5. Lattice distortion in RHEA

A recent investigation by Lee et al. [50] reveals that the VNbTaTiZr HEA exhibits higher yield strength and comparable plasticity when compared to VNbTaTi HEA. The increase in yield strength is analyzed concerning lattice distortion, employing a combination of theoretical modeling, first-principles calculations, synchrotron X-ray/neutron diffraction, atom-probe tomography, and scanning transmission electron microscopy techniques. These findings underscore the pivotal role of severe lattice distortion in affecting the strength of refractory HEAs. Theoretical calculations of the primary strengthening components suggest that the high strength observed in both the VNbTaTi and VNbTaTiZr HEAs is primarily attributed to lattice mismatch, rather than modulus mismatch [51]. Consequently, it can be inferred that solid-solution strengthening is primarily driven by the lattice-distortion effect. The incorporation of Zr efficiently induces a distorted lattice, resulting in substantially higher yield strength in the alloy compared to the VNbTaTi HEA.

To determine if the current MEAM potential shows a similar relationship between strength and lattice distortion, the latter (\bar{u}^D) is computed using the following equation to determine the lattice-distortion factor following the methodology outlined by Lee et al. [50]:

$$\bar{u}^D = \sqrt{\sum_i^n (d_i^{eff} - \bar{d})^2} \quad (3.8)$$

Here, d_i^{eff} represents the effective interatomic distance of the i th element, \bar{d} signifies the average interatomic distance of n elements, determined from the lattice constant of the constituent elements associated with their respective crystal structure, and n denotes the number of constituent elements. Table 6 presents the results for this parameter obtained with the current MEAM, alongside previous DFT calculations and experiments. While slight variations in absolute values may be attributed to temperature effects, the overall trend derived from the MEAM potential aligns notably well with observations from DFT and experimental studies. This provides strong validation for the development of the potential and underscores its efficacy in investigating the influence of Zr on the deformation mechanism of this RHEA. For a more in-depth mathematical understanding of the lattice distortion factor calculation, readers are encouraged to refer to the work by Lee et al. [50].

3.2. Mechanical behavior

3.2.1. Deformation behavior in single crystal RHEA: Uniaxial strain tension

The present MEAM potential for the RHEA system was rigorously validated under simulated mechanical loading conditions. This is crucial to ensure the potential accurately captures the alloy behavior under the high stresses and strains encountered during plastic deformation.

The validation specifically involved uniaxial (strain) tension simulations to probe the mechanical response and deformation mechanisms in the RHEA, mainly the capability of the potential to reproduce deformation twinning under high strain rates.

The simulation box creation involved a parent BCC Ta crystal, characterized by lattice constants of 3.3 \AA , and oriented along the $x \parallel [100]$, $y \parallel [010]$, and $z \parallel [001]$ axes. The study examines the dynamic response of VNbTaTi and VNbTaTiZr alloys under uniaxial deformation, employing a simulation cell measuring 7 nm \times 7 nm \times 30 nm, with approximately 100,000 atoms. Subsequently, a pseudo-random substitution process was employed to replace Ta atomic sites with equiatomic compositions of 25% V, Nb, Ta, Ti and 20% V, Nb, Ta, Ti, Zr thus forming the HEA. Two distinct strain rates along the z axis, $10^8/\text{s}$ and $10^9/\text{s}$, are applied to analyze the mechanical behavior of both HEAs. Two microstructure variants of the HEAs are considered: the as-cast (Ran-HEA) configuration, characterized by a random atom distribution, and the homogenized via Monte Carlo (MC-HEA), where atom segregation is evident (Fig. 4(a-d)). The Ran-HEA systems underwent minimization using the conjugate gradient method, and equilibration to ambient conditions (300 K, zero pressure) was achieved through an isothermal-isobaric ensemble (NPT).

To characterize twins, the Virtual Texture Analysis tool (VirTex) [52] was employed. This tool utilizes quaternion angles derived from OVITO's [53] Polyhedral Template Matching (PTM) technique [54], employing a root-mean-square deviation (RMSD) threshold of 0.2. Additionally, local atomic structural information was obtained using the Common Neighbor Analysis method integrated within PTM. The quaternion data was further transformed into rotation matrices using VirTex to represent crystal orientations relative to a reference coordinate system. The pivotal plane of twin systems was determined by normalizing the components of the third column of the rotation matrix (Normal Direction), while the direction was ascertained through the first column (Rolling Direction).

The as-cast (Ran-HEA) configuration and the homogenized MC (MC-HEA) configurations were examined at $10^9/\text{s}$ and $10^8/\text{s}$ strain rates, and the reference Nb, Ta, NbTa, and NbTaTi were probed at $10^9/\text{s}$, as illustrated in Fig. 5. The addition of Ti and Zr are observed to weaken the material, as these show a lower peak stress than the pure elements, as well as NbTa. Moreover, the VNbTaTi has a higher yield strength since the Ti content is only 25%, whereas in NbTaTi is ~33%. Lower strain rates exhibit strain hardening after an initial softening phase—additionally, the inclusion of Zr results in virtually no drop in stress post-yield.

A distinctive behavior is observed in the HEA where the primary mode of deformation is twinning. The initiation of twins before yield in these HEAs can be elucidated by stress-state-dependent behavior, with tension being the favored loading condition for twin formation. Under tension, the stresses facilitate the shearing of atomic planes along specific crystallographic directions, enabling the material to accommodate deformation through twins. A detailed examination of the twin evolution for the systems at a strain rate of $10^9/\text{s}$ is presented in Fig. 6. The addition of elements into the alloy results in a more amorphous twinned region as compared to the pure elements or the NbTa and NbTaTi systems (Fig. 6, top), however, all systems show that the same twin types are active during deformation (Fig. 6, bottom). Here, snapshots were selected at the same strain, and the twin type was characterized by the VirTex tool. The HEA shows the same twin core structures as the pure elements, with the most active systems being $\{111\}\{112\}$ and $\{135\}\{135\}$. The presence of elemental segregation in the HEA shows no significant barrier for twin nucleation, but it might affect the growth of the twins. The distinct twin systems characterized have been previously documented in both experimental studies of BCC-based HEA materials [55–58] and pure BCC metals [59–61]. Furthermore, the inclusion of Zr, resulting in no clear yield point, can be further explained by the sustained nucleation of intertwined twins, contributing to enhanced ductility, as an abundance of twin boundaries collectively mitigate stress concentrations during deformation [55].

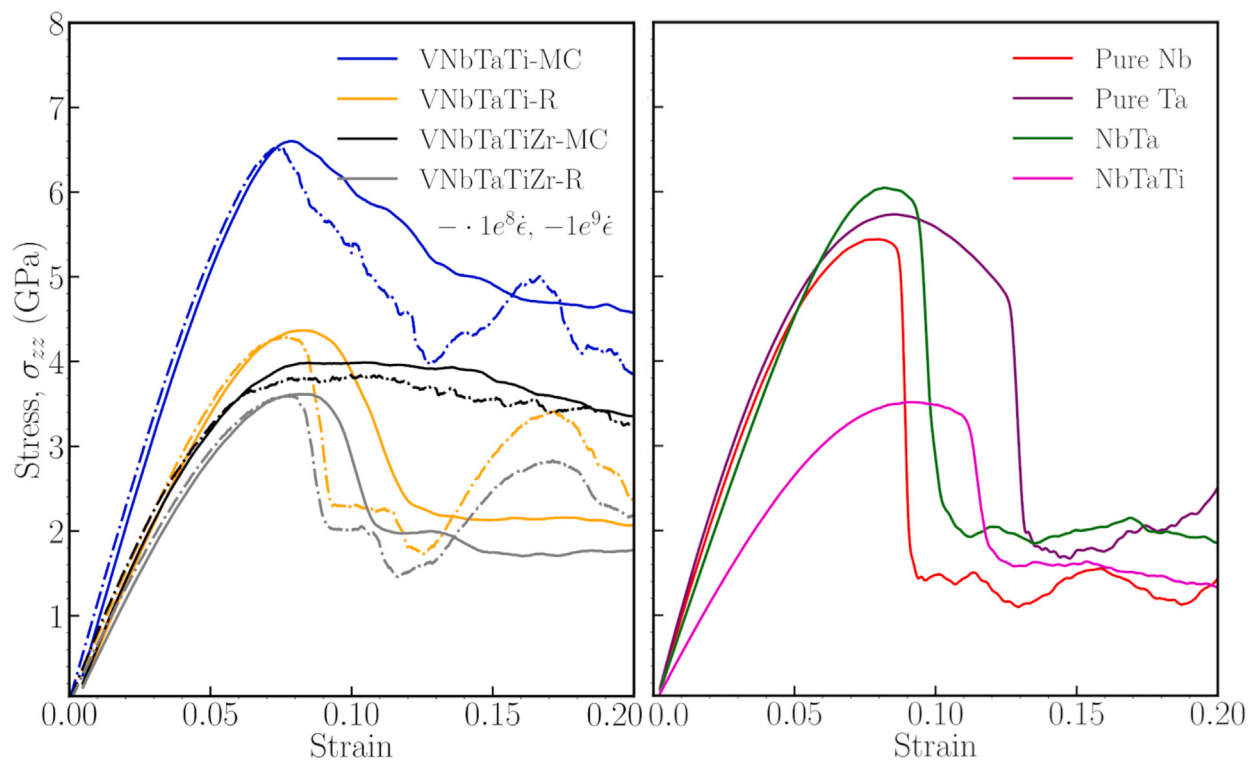


Fig. 5. Stress-strain curve of single crystal VNbTaTi and VNbTaTiZr at $10^8/\text{s}$ (dash-dot lines) and $10^9/\text{s}$ (solid lines) strain rates in uniaxial strain tension (left), and reference Nb, Ta, NbTa, and NbTaTi at $10^9/\text{s}$ strain rate (right).

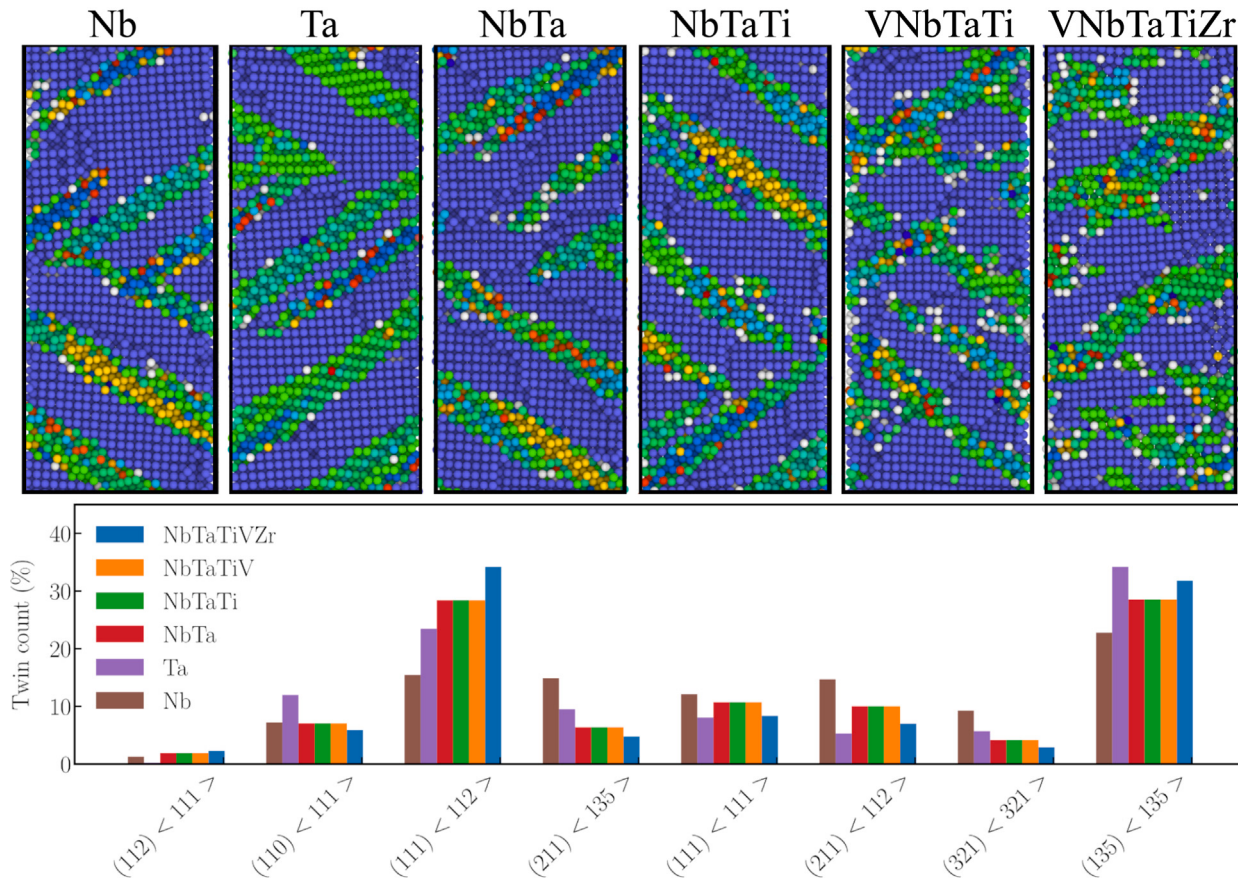


Fig. 6. Illustrative microstructures of twins, and quantification of twin variants in single crystal (sc) systems. Snapshots for the analysis are taken at an elongation of 13%. Bulk BCC atoms and twin boundaries are not considered in the quantification of twins. BCC atoms are colored blue, and the twinned regions are colored based on relative orientation to highlight twins.

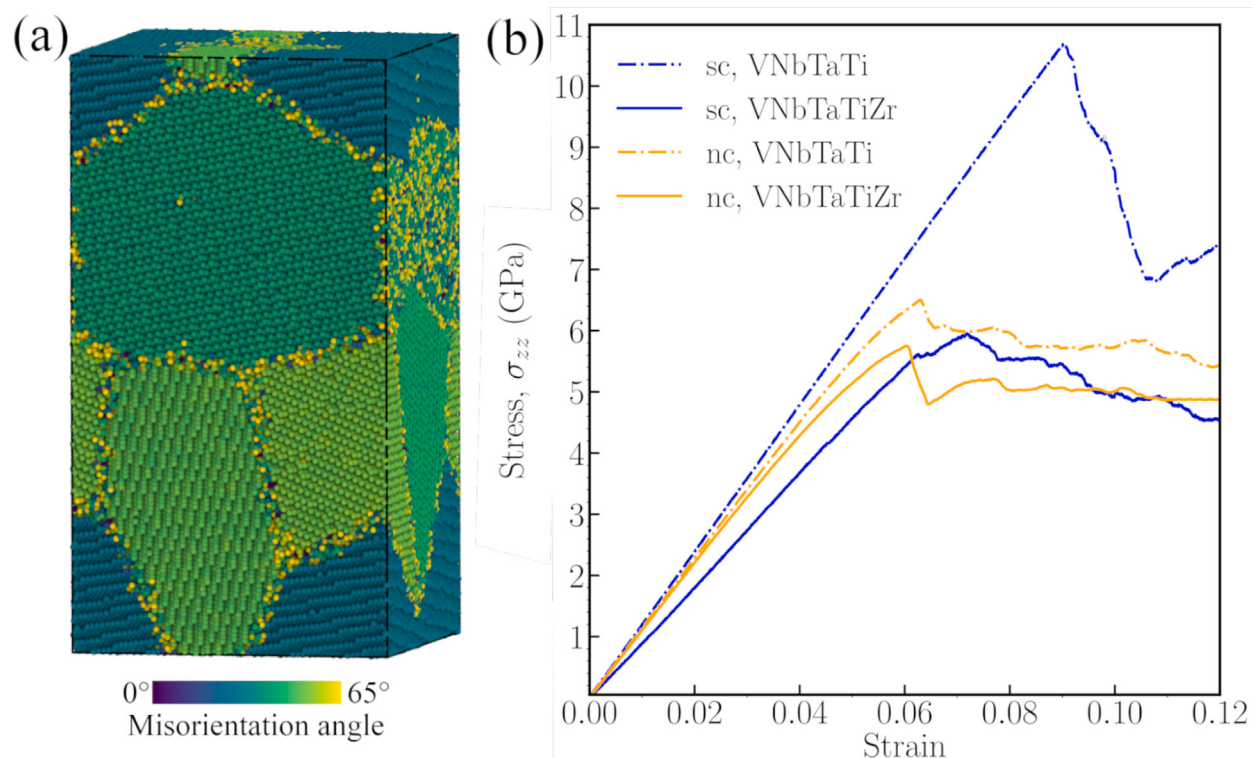


Fig. 7. (a) Microstructure of *nc* simulation cell used for uniaxial strain loading colored based on misorientation angle using OVITO. (b) Stress–strain curve of *sc* and *nc* RHEAs at $10^8/\text{s}$ strain rate.

3.2.2. Deformation behavior in nano-crystal RHEA: Uniaxial strain compression

The study was also used to investigate if the same twinning deformation mode is observed in compression tests, a single crystal (*sc*) system oriented along the $x \parallel [1\ 0\ 0]$, $y \parallel [0\ 1\ 0]$, and $z \parallel [0\ 0\ 1]$ axes, and a nano-crystal(*nc*) with random crystal orientations for each grain are probed in the VNbTaTi and VNbTaTiZr RHEA configurations. The methodology for the Monte Carlo was the same as in the tensile test simulation cells, and the size for the *sc* was kept the same. The *nc* is purposefully built for larger dimensions (measuring $20\text{ nm} \times 20\text{ nm} \times 40\text{ nm}$) to have large enough grains (five $\sim 17\text{ nm}$ grains), resulting in approximately 890,000 atoms as depicted in Fig. 7(a).

The systems were loaded at a strain rate of $10^8/\text{s}$, resulting in the stress–strain curve in Fig. 7(b). In *sc*, VNbTaTi has a higher peak stress than VNbTaTiZr, attributed to the additional segregations due to the addition of Zr that serve as dislocation barriers. These segregations can then serve to entangle dislocations, making further movement of the material as a result of the deformation more difficult. This is represented by the strain softening in VNbTaTi after yield, whereas the addition of Zr shows strain hardening after yield. Moreover, no twinning phenomenon was observed in *sc*, in line with some experimental findings suggesting that the deformation mechanism in these HEAs primarily involves a slip-mediated process, giving rise to the larger generation of dislocations over twin nucleation [51,62], e.g. by generation of large slip bands [63].

The disparity between *sc* and *nc* is associated with the presence of grain boundaries, which, similar to the addition of Zr in *sc*, serve as barriers for dislocation motion. This is supported by the lower peak stress in *nc* and the smaller drop in stress after yield. Additionally, this deformation is observed to be a twin-mediated process, as depicted in the microstructural slices in Fig. 8 showing type-I twins, as reported in recent experimental work on *nc*-VNbTaTi at room RT and a strain rate of $10^3/\text{s}$ [63]. Twins are observed to nucleate in both grain interior and at grain boundaries, however, thicker and more stable twins were observed to nucleate from the grain boundaries, as depicted in the twin

evolution at various strains in Fig. 8. This is also observed in the *nc* VNbTaTiZr, however, more needle-like and longer twins are observed. The different twin morphology and mechanical response between *sc* and *nc* is attributed not only to the variety of crystal orientations and orientation relationships in the latter [59–61], but also to the grain boundaries acting as nucleation for twins and as barriers for twin motion, leading to different twin network morphology and evolution in *nc*.

3.2.3. Strength control in RHEAs through edge dislocations

Recent studies have highlighted the strength and high-temperature performance of RHEAs, particularly in materials like VNbTaTi. Surprisingly, it has been discovered that edge dislocations, rather than the expected screw dislocations, play a crucial role in controlling plastic flow [64,65]. This is in contrast to BCC alloys, where screw dislocations dominate in metals and dilute alloys [66,67]. Theoretical work by Maresca and Curtin [64] has proposed that complex RHEAs exhibit unique behavior, where each alloying element interacts with dislocations. This leads to dislocations adopting a low-energy wavy structure, allowing them to navigate through low-energy solute areas and avoid high-energy regions. The plastic flow then requires thermal activation of dislocations that have to overcome barriers created by adjacent high-energy environments. A guided computational search for advanced alloys that can tailor the dislocation motion based on local atomic arrangement, offers a promising approach for the engineering of new alloys. Surprisingly, despite the potential benefits at the atomic level, this particular investigation has not been undertaken due to the absence of an accurate force field.

Here, the effect of edge dislocation nucleation and motion on the strength of VNbTaTiZr and subsystems was also investigated since the characteristics of dislocation in metals are intrinsically linked to the Peierls stress. This stress represents the resolved shear stress necessary to mobilize a dislocation within its glide plane. To explore this, the Peierls barrier for existing dislocations in VNbTaTiZr RHEA and its subsystem was computed and compared to experimental data [67,68].

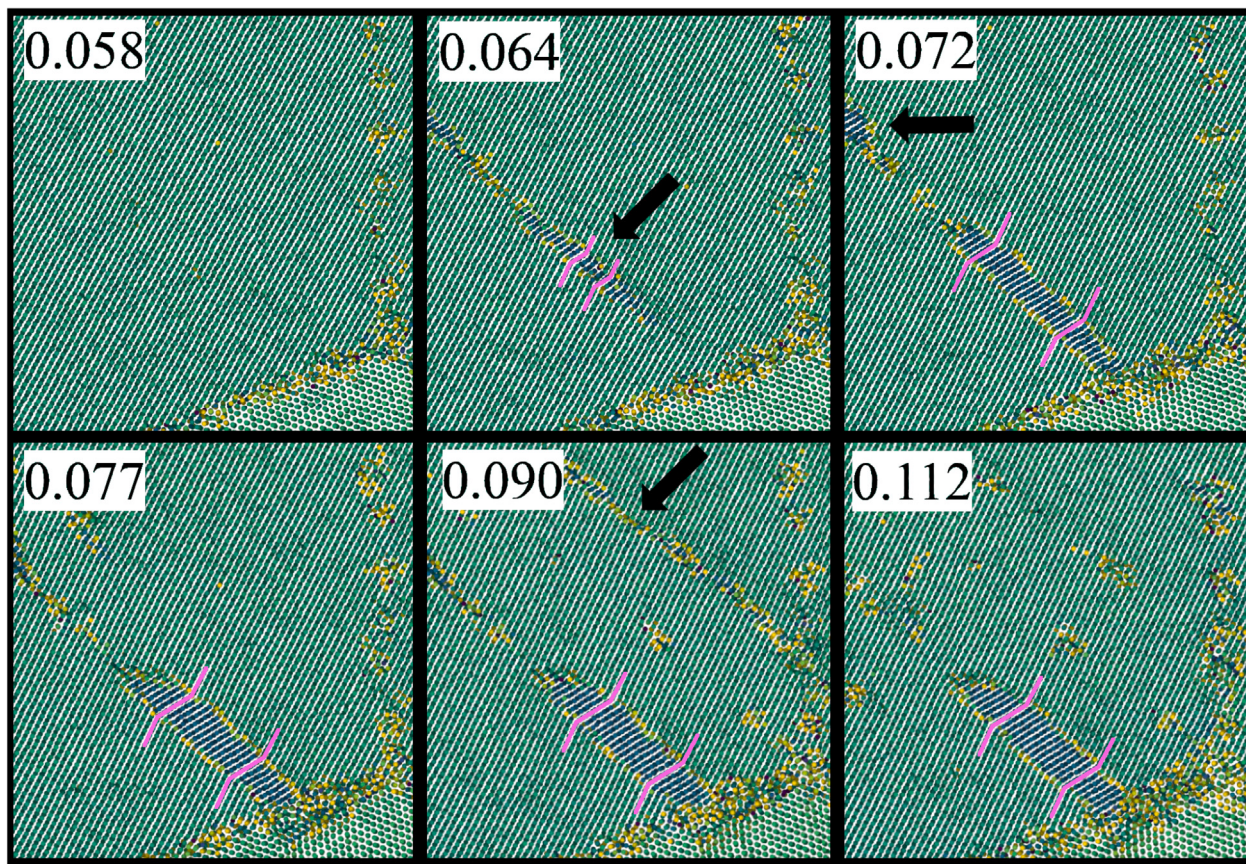


Fig. 8. Microstructural images showing the evolution of twins at different strains during uniaxial tension deformation. The pink lines denote the twin and matrix lines in the more stable twin, and the black arrows highlight twin locations.

The Peierls stress was determined using the Periodic Array of Dislocations (PAD) model. Table 7 provides detailed information on the number of atoms, crystallographic orientations, and initial dimensions of the simulation cells (L_x , L_y , L_z) for the models. An edge or a screw dislocation, characterized by a Burgers vector of $\vec{b} = (a_0/2) \{111\}$, was introduced at the center of the simulation cell [69,70]. This was accomplished by the ATOMMAN python package (the source code is accessible at <https://github.com/usnistgov/atomman>). For all Peierls stress calculations, MS simulations are conducted at 0K. The dislocation line was aligned with the x -axis, and the $y-x$ plane was defined as the slip plane where the dislocation was positioned. Periodic boundary conditions were applied in both x and y directions, while non-periodic and fixed boundary conditions were set in the z direction. Fig. 9(a-b) illustrates the shear direction and orientation for both edge and screw dislocations. Furthermore, Fig. 9(c) shows the core structures of four dislocations (edge and screw $\{111\}$ dislocation in two planes $\{110\}$ and $\{112\}$) in the VNbTaTiZr alloy following the MC simulation. A progressive strain tensor, ϵ is applied, inducing a gradual deformation of the simulation cell from an initial cuboidal shape to a triclinic form. The non-zero shear strain component in the case of a screw dislocation is denoted as ϵ_{xy} , and as ϵ_{yz} for an edge dislocation. All remaining strain components were zero. The strain was increased in increments of 1×10^{-5} for all dislocations until a maximum strain of 0.3. After each incremental strain, the simulation cell was minimized using a conjugate gradient, following the same process as previously described.

In pure BCC metals like tantalum, plastic deformation at low temperatures is controlled by the motion of straight screw dislocations. A screw dislocation line moves perpendicular to its length by nucleating pairs of “kinks” that propagate in opposite directions along the line. In dilute BCC alloys, both screw and edge dislocations interact with solute atoms. However, the interaction is strongest for screw dislocations

because solute atoms promote the formation of “superjogs” that act as strong pinning points [68]. The friction stress on edge dislocations also increases with solute content but remains below the applied stress. Thus, deformation is still controlled by screw dislocation motion even in dilute BCC alloys [67,71,72]. For example, the shear strength for an edge dislocation in pure tantalum, shown in Table 8, that glides on the $\{110\}$ and $\{112\}$ planes is 83 and 131 MPa respectively, much lower than the shear strengths of 632 and 876 MPa for screw dislocation glide on those same planes.

In contrast, for refractory RHEAs with high solute concentrations, the required shear stress to move edge dislocations is large and comparable to the one for screw dislocations (see Table 8). Thus, it appears that edge dislocations contribute to the plastic deformation in these complex concentrated alloys. The high solute concentration leads to inhomogeneous distributions of locally ordered structures that can pin and influence the mobilities of both screw and edge dislocations [73, 74]. Importantly, previous studies have shown that, unlike screw, edge dislocations can relax into a wavy low-energy configuration, providing barriers to thermally-activated glide of the edge dislocations over distances related to the characteristic lengths of the waviness [64].

Table 8 shows that in equiatomic RHEAs like VNbTaTi, and VNbTaTiZr, the Peierls stress for edge dislocation glide is higher than for screw dislocation glide on both the $\{110\}$ and $\{112\}$ planes. Maresca and Curtin [64] proposed that the random solute distribution enables substantial strengthening of the edge dislocations. The trapping of edge dislocations in favorable solute environments creates large intrinsic barriers to their motion. Atomistic simulations using appropriate interatomic potentials for the VNbTaTi alloy confirm this hypothesis. The new MEAM potential reproduces the experimentally observed strength and supports the theory that attributes the strength to the complex atomic-scale randomness of the high entropy alloy [62]. Overall, the

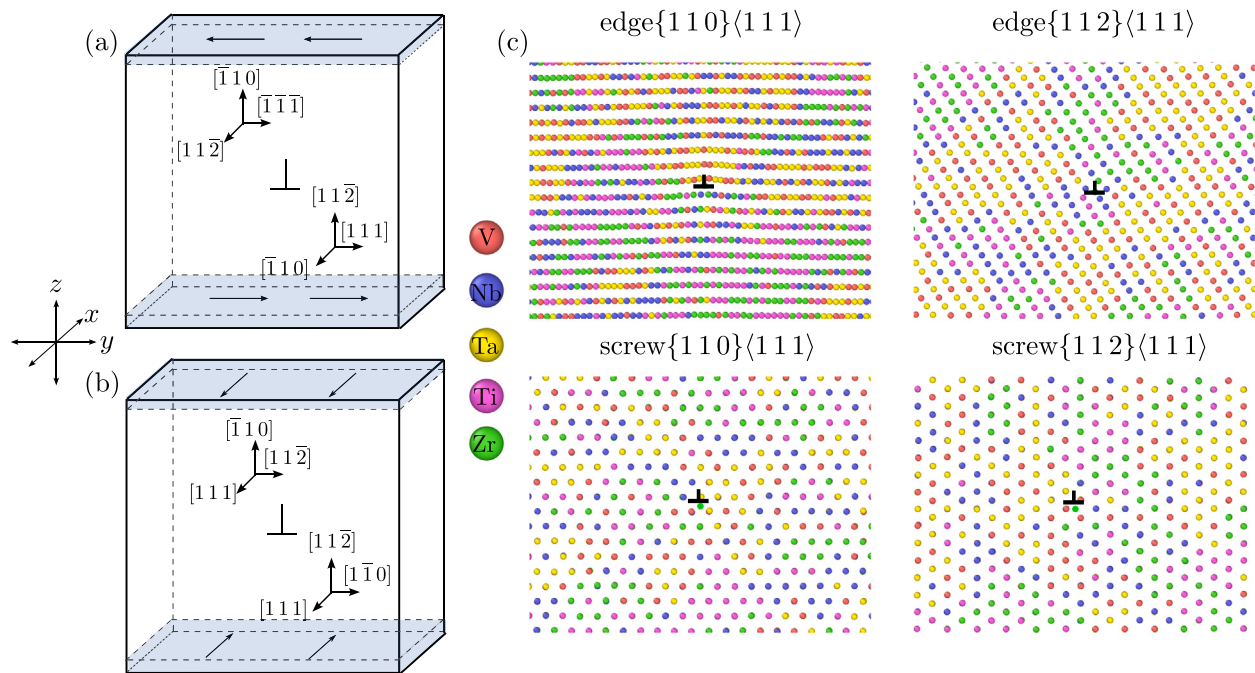


Fig. 9. (a–b) Schematic illustrating shear loading plane and direction for (a) edge and (b) screw dislocation and (c) dislocation core structure in VNbTaTiZr HEA for both screw and edge ($a_0/2\{111\}$) dislocations in $\{110\}$ and $\{112\}$ planes.

Table 7

The number of atoms, crystallographic orientations, and edge lengths for each simulation cell to calculate the Peierls stress.

Plane	Dislocation	No. of atoms	x	y	z	L_x (Å)	L_y (Å)	L_z (Å)
$\{110\}$	Edge	71 982	$[1\bar{1}\bar{2}]$	$[\bar{1}\bar{1}1]$	$[\bar{1}10]$	8.07	398.28	400.94
	Screw	51 600	$\{111\}$	$[1\bar{1}\bar{2}]$	$[\bar{1}10]$	5.73	403.14	400.38
$\{112\}$	Edge	83 700	$[\bar{1}10]$	$\{111\}$	$[11\bar{2}]$	9.28	398.69	404.67
	Screw	51 600	$\{111\}$	$[\bar{1}10]$	$[11\bar{2}]$	5.73	400.33	403.24

Table 8

Calculated Peierls stress (in MPa) for both screw and edge ($a_0/2\{111\}$) dislocations in $\{110\}$ and $\{112\}$ planes using the present MEAM potential for pure Ta, as well as for two RHEAs (VNbTaTi and VNbTaTiZr). It should be noted that an average of five Peierls stress calculations are conducted to ensure the robustness of current findings against the local atomic environment's variability. This approach has confirmed that the observed differences in Peierls stress between edge and screw dislocations are statistically significant, thereby reinforcing the validity of current results. Additionally, the error margins are specified.

Component	Dislocation type	Plane		
			$\{110\}$	$\{112\}$
Ta	Edge	10	64	
	Screw	630	855	
VNbTaTi	Edge	1161 ± 20	1393 ± 12	
	Screw	769 ± 8	943 ± 15	
VNbTaTiZr	Edge	987 ± 17	1454 ± 29	
	Screw	791 ± 18	803 ± 11	

results indicate that edge dislocations govern plastic deformation in BCC HEAs, unlike in dilute BCC alloys where screw dislocations remain dominant.

4. Conclusion

In this work, a new MEAM potential was developed to model the VNbTaTiZr and subsystems refractory RHEAs. The potential parameters were fit to an extensive database of DFT data on lattice constants, elastic constants, stacking faults, etc. The potential accurately reproduces the DFT results for:

- Lattice constants and elastic constants of the RHEA and its subsystems
- Generalized stacking fault energies for different slip planes
- Short-range chemical ordering effects from Monte Carlo simulations
- Lattice distortion trends when adding Zr to VNbTaTi

Molecular dynamics simulations using the potential validate new insights into deformation mechanisms:

- Under compressive loading, dislocation slip dominates over twinning in the RHEA, unlike pure BCC metals where deformation twinning is prevalent
- Under tensile loading, deformation twinning is favored and the RHEA shows activation of the same twin modes as pure BCC elements
- Edge dislocations exhibit higher Peierls stresses than screw dislocations, indicating they govern plastic flow in the RHEA unlike dilute BCC alloys

The validated potential enables future large-scale atomistic studies to uncover atomic-level origins of exceptional strength, ductility, and high-temperature stability in the VNbTaTiZr RHEA. The advanced potential lays the groundwork for the computational design of new RHEAs and multi-principal element alloys with targeted mechanical properties by leveraging atomic-scale insights into structure–property relationships. Overall, linking first-principles data to a robust interatomic potential model creates new opportunities for mechanistic discovery in this important class of high-performance structural materials

CRediT authorship contribution statement

Mashroor S. Nitol: Writing – original draft, Validation, Software, Methodology, Formal analysis, Conceptualization. **Marco J. Echeverria:** Writing – original draft, Visualization, Validation, Software, Investigation, Formal analysis, Conceptualization. **Khanh Dang:** Review, Conceptualization. **Michael I. Baskes:** Writing – review & editing, Supervision, Methodology. **Saryu J. Fensin:** Writing – review & editing, Project administration, Funding acquisition.

Declaration of competing interest

The authors declare that they have no known competing financial interests or personal relationships that could have appeared to influence the work reported in this paper.

Data availability

The potentials can be accessed on the NIST website <https://www.ctcms.nist.gov/potentials/>.

References

- [1] J.-W. Yeh, S.-K. Chen, S.-J. Lin, J.-Y. Gan, T.-S. Chin, T.-T. Shun, C.-H. Tsau, S.-Y. Chang, Nanostructured high-entropy alloys with multiple principal elements: novel alloy design concepts and outcomes, *Adv. Eng. Mater.* 6 (5) (2004) 299–303.
- [2] O.N. Senkov, G. Wilks, J. Scott, D.B. Miracle, Mechanical properties of Nb25Mo25Ta25W25 and V20Nb20Mo20Ta20W20 refractory high entropy alloys, *Intermetallics* 19 (5) (2011) 698–706.
- [3] Z. Lei, X. Liu, Y. Wu, H. Wang, S. Jiang, S. Wang, X. Hui, Y. Wu, B. Gault, P. Kontis, et al., Enhanced strength and ductility in a high-entropy alloy via ordered oxygen complexes, *Nature* 563 (7732) (2018) 546–550.
- [4] B. Gludovatz, A. Hohenwarter, D. Catoor, E.H. Chang, E.P. George, R.O. Ritchie, A fracture-resistant high-entropy alloy for cryogenic applications, *Science* 345 (6201) (2014) 1153–1158.
- [5] M.-H. Tsai, J.-W. Yeh, High-entropy alloys: a critical review, *Mater. Res. Lett.* 2 (3) (2014) 107–123.
- [6] C. Zhang, F. Zhang, H. Diao, M.C. Gao, Z. Tang, J.D. Poplawsky, P.K. Liaw, Understanding phase stability of Al-Co-Cr-Fe-Ni high entropy alloys, *Mater. Des.* 109 (2016) 425–433.
- [7] H. Yao, J. Qiao, J. Hawk, H. Zhou, M. Chen, M. Gao, Mechanical properties of refractory high-entropy alloys: Experiments and modeling, *J. Alloys Compd.* 696 (2017) 1139–1150.
- [8] C. Lee, G. Song, M.C. Gao, R. Feng, P. Chen, J. Brechtl, Y. Chen, K. An, W. Guo, J.D. Poplawsky, et al., Lattice distortion in a strong and ductile refractory high-entropy alloy, *Acta Mater.* 160 (2018) 158–172.
- [9] B.-J. Lee, M. Baskes, H. Kim, Y.K. Cho, Second nearest-neighbor modified embedded atom method potentials for bcc transition metals, *Phys. Rev. B* 64 (18) (2001) 184102.
- [10] W.-M. Choi, Y.H. Jo, S.S. Sohn, S. Lee, B.-J. Lee, Understanding the physical metallurgy of the CoCrFeMnNi high-entropy alloy: an atomistic simulation study, *Npj Comput. Mater.* 4 (1) (2018) 1.
- [11] D. Farkas, A. Caro, Model interatomic potentials for Fe–Ni–Cr–Co–Al high-entropy alloys, *J. Mater. Res.* 35 (22) (2020) 3031–3040.
- [12] W.-M. Choi, Y. Kim, D. Seol, B.-J. Lee, Modified embedded-atom method interatomic potentials for the Co-Cr, Co-Fe, Co-Mn, Cr-Mn and Mn-Ni binary systems, *Comput. Mater. Sci.* 130 (2017) 121–129.
- [13] Y.-K. Kim, W.-S. Jung, B.-J. Lee, Modified embedded-atom method interatomic potentials for the Ni–Co binary and the Ni–Al–Co ternary systems, *Modelling Simul. Mater. Sci. Eng.* 23 (5) (2015) 055004.
- [14] X. Duan, J. Guo, L. Chen, Z. Zhang, X. Huang, L. Liu, B. Shan, Atomistic simulation of local chemical order in NbTiZrMoV high entropy alloy based on a newly-developed interatomic potential, *Comput. Mater. Sci.* 227 (2023) 112269.
- [15] X. Huang, L. Liu, X. Duan, W. Liao, J. Huang, H. Sun, C. Yu, Atomistic simulation of chemical short-range order in HfNbTaZr high entropy alloy based on a newly-developed interatomic potential, *Mater. Des.* 202 (2021) 109560.
- [16] B.-J. Lee, J.-H. Shim, M. Baskes, Semiempirical atomic potentials for the fcc metals Cu, Ag, Au, Ni, Pd, Pt, Al, and Pb based on first and second nearest-neighbor modified embedded atom method, *Phys. Rev. B* 68 (14) (2003) 144112.
- [17] S.B. Maisel, W.-S. Ko, J.-L. Zhang, B. Grabowski, J. Neugebauer, Thermomechanical response of NiTi shape-memory nanoprecipitates in TiV alloys, *Phys. Rev. Mater.* 1 (3) (2017) 033610.
- [18] Y.-M. Kim, B.-J. Lee, M. Baskes, Modified embedded-atom method interatomic potentials for Ti and Zr, *Phys. Rev. B* 74 (1) (2006) 014101.
- [19] R. Storn, K. Price, Differential evolution-a simple and efficient heuristic for global optimization over continuous spaces, *J. Glob. Optim.* 11 (4) (1997) 341.
- [20] Y.-K. Kim, H.-K. Kim, W.-S. Jung, B.-J. Lee, Atomistic modeling of the Ti-Al binary system, *Comput. Mater. Sci.* 119 (2016) 1–8.
- [21] T. Wang, Z. Jin, J.-C. Zhao, Thermodynamic assessment of the Al-Zr binary system, *J. Phase Equilibil.* 22 (2001) 544–551.
- [22] A.P. Thompson, H.M. Aktulga, R. Berger, D.S. Bolintineanu, W.M. Brown, P.S. Crozier, P.J. in 't Veld, A. Kohlmeyer, S.G. Moore, T.D. Nguyen, R. Shan, M.J. Stevens, J. Tranchida, C. Trott, S.J. Plimpton, LAMMPS - a flexible simulation tool for particle-based materials modeling at the atomic, meso, and continuum scales, *Comput. Phys. Comm.* 271 (2022).
- [23] G. Kresse, J. Hafner, Norm-conserving and ultrasoft pseudopotentials for first-row and transition elements, *J. Phys.: Condens. Matter* 6 (40) (1994) 8245.
- [24] G. Kresse, J. Furthmüller, Efficiency of ab-initio total energy calculations for metals and semiconductors using a plane-wave basis set, *Comput. Mater. Sci.* 6 (1) (1996) 15–50.
- [25] J.P. Perdew, K. Burke, M. Ernzerhof, Generalized gradient approximation made simple, *Phys. Rev. Lett.* 77 (18) (1996) 3865.
- [26] P.E. Blöchl, Projector augmented-wave method, *Phys. Rev. B* 50 (24) (1994) 17953.
- [27] H. Ikehata, N. Nagasako, T. Furuta, A. Fukumoto, K. Miwa, T. Saito, First-principles calculations for development of low elastic modulus Ti alloys, *Phys. Rev. B* 70 (17) (2004) 174113.
- [28] D. Farkas, C. Jones, Interatomic potentials for ternary Nb-Ti-Al alloys, *Modelling Simul. Mater. Sci. Eng.* 4 (1) (1996) 23.
- [29] B.-T. Wang, W.-D. Li, P. Zhang, First-principles calculations of phase transition, elasticity, and thermodynamic properties for TiZr alloy, *J. Nuclear Mater.* 420 (1–3) (2012) 501–507.
- [30] A. Zunger, S.-H. Wei, L. Ferreira, J.E. Bernard, Special quasirandom structures, *Phys. Rev. Lett.* 65 (3) (1990) 353.
- [31] A. Van De Walle, M. Asta, G. Ceder, The alloy theoretic automated toolkit: A user guide, *CALPHAD* 26 (4) (2002) 539–553.
- [32] S. Xu, E. Hwang, W.-R. Jian, Y. Su, I.J. Beyerlein, Atomistic calculations of the generalized stacking fault energies in two refractory multi-principal element alloys, *Intermetallics* 124 (2020) 106844.
- [33] R. Hill, The elastic behaviour of a crystalline aggregate, *Proc. Phys. Soc. A* 65 (5) (1952) 349.
- [34] L. Yang, K. Xiong, H. Dai, H. Wu, S. Zhang, Y. Wang, J. He, Y. Mao, An ambient ductile VnBta refractory medium-entropy alloy with super rolling formability, *Mater. Sci. Eng. A* (2023) 145841.
- [35] R. Feng, G. Kim, D. Yu, Y. Chen, W. Chen, P.K. Liaw, K. An, Elastic behavior of binary and ternary refractory multi-principal-element alloys, *Mater. Des.* 219 (2022) 110820.
- [36] S. Rao, B. Akdim, E. Antillon, C. Woodward, T. Parthasarathy, O. Senkov, Modeling solution hardening in BCC refractory complex concentrated alloys: NbTiZr, Nb1. 5TiZr0. 5 and Nb0. 5TiZr1. 5, *Acta Mater.* 168 (2019) 222–236.
- [37] C. Lee, G. Kim, Y. Chou, B.L. Musicó, M.C. Gao, K. An, G. Song, Y.-C. Chou, V. Keppens, W. Chen, et al., Temperature dependence of elastic and plastic deformation behavior of a refractory high-entropy alloy, *Sci. Adv.* 6 (37) (2020) eaaz4748.
- [38] F. Tian, L.K. Varga, N. Chen, J. Shen, L. Vitos, Ab initio design of elastically isotropic TiZrNbMoV high-entropy alloys, *J. Alloys Compd.* 599 (2014) 19–25.
- [39] L. Shao, C.-R. Xu, N. Ding, X.-T. Chen, J.-M. Duan, B.-Y. Tang, The intrinsic mechanical properties of NbTaTiZr and the influence of alloying elements Mo and W: A first-principles study, *J. Alloys Compd.* 911 (2022) 165109.
- [40] K. Limmer, J.E. Medvedeva, D.C. Van Aken, N. Medvedeva, Ab initio simulation of alloying effect on stacking fault energy in fcc fe, *Comput. Mater. Sci.* 99 (2015) 253–255.
- [41] A. Hunter, I.J. Beyerlein, T.C. Germann, M. Koslowski, Influence of the stacking fault energy surface on partial dislocations in fcc metals with a three-dimensional phase field dislocations dynamics model, *Phys. Rev. B* 84 (14) (2011) 144108.
- [42] S.M. Shaikh, B. Murty, S.K. Yadav, On the influence of enthalpy of formation on lattice distortion and intrinsic ductility of concentrated refractory alloys, *J. Appl. Phys.* 134 (3) (2023).
- [43] B. Akdim, C. Woodward, S. Rao, E. Antillon, Predicting core structure variations and spontaneous partial kink formation for $1/2 < 111 >$ screw dislocations in three BCC NbTiZr alloys, *Scr. Mater.* 199 (2021) 113834.
- [44] G. Anand, S. Ghosh, M. Eisenbach, Order parameter engineering for random systems, *High Entropy Alloys Mater.* (2023) <http://dx.doi.org/10.1007/s44210-023-00015-x>.
- [45] J.M. Cowley, An approximate theory of order in alloys, *Phys. Rev.* 77 (1950) 669–675, <http://dx.doi.org/10.1103/PhysRev.77.669>.
- [46] I.J. Beyerlein, P. Cao, T.M. Pollock, Complex concentrated alloys and chemical short-range ordering, *MRS Bull.* 48 (7) (2023) 746–752, <http://dx.doi.org/10.1557/s43577-023-00567-8>.
- [47] R. Salloom, M.I. Baskes, S.G. Srinivasan, Atomic level simulations of the phase stability and stacking fault energy of FeCoCrMnSi high entropy alloy, *Modelling Simul. Mater. Sci. Eng.* 30 (7) (2022) 075002, <http://dx.doi.org/10.1088/1361-651X/ac860d>.

- [48] D. de Fontaine, The number of independent pair-correlation functions in multi-component systems, *J. Appl. Crystallogr.* 4 (1) (1971) 15–19, <http://dx.doi.org/10.1107/S0021889871006174>.
- [49] M.C. Troparevsky, J.R. Morris, M. Daene, Y. Wang, A.R. Lupini, G.M. Stocks, Beyond atomic sizes and hume-rothery rules: Understanding and predicting high-entropy alloys, *JOM* 67 (10) (2015) 2350–2363, <http://dx.doi.org/10.1007/s11837-015-1594-2>.
- [50] C. Lee, Y. Chou, G. Kim, M.C. Gao, K. An, J. Brechtl, C. Zhang, W. Chen, J.D. Poplawsky, G. Song, Y. Ren, Y.-C. Chou, P.K. Liaw, Lattice-distortion-enhanced yield strength in a refractory high-entropy alloy, *Adv. Mater.* 32 (49) (2020) 2004029, [Online]. Available: <https://onlinelibrary.wiley.com/doi/abs/10.1002/adma.202004029>.
- [51] C. Lee, G. Song, M.C. Gao, R. Feng, P. Chen, J. Brechtl, Y. Chen, K. An, W. Guo, J.D. Poplawsky, S. Li, A. Samaei, W. Chen, A. Hu, H. Choo, P.K. Liaw, Lattice distortion in a strong and ductile refractory high-entropy alloy, *Acta Mater.* 160 (2018) 158–172, [Online]. Available: <https://www.sciencedirect.com/science/article/pii/S1359645418306906>.
- [52] A. Mishra, M.J. Echeverria, K. Ma, S. Parida, C. Chen, S. Galitskiy, A.M. Dongare, Virtual texture analysis to investigate the deformation mechanisms in metal microstructures at the atomic scale, *J. Mater. Sci.* 57 (23) (2022) 10549–10568.
- [53] A. Stukowski, Visualization and analysis of atomistic simulation data with OVITO—the open visualization tool, *Modelling Simul. Mater. Sci. Eng.* 18 (1) (2010).
- [54] P.M. Larsen, S. Schmidt, J. Schiøtz, Robust structural identification via polyhedral template matching, *Modelling Simul. Mater. Sci. Eng.* 24 (5) (2016).
- [55] E.P. George, W.A. Curtin, C.C. Tasan, High entropy alloys: A focused review of mechanical properties and deformation mechanisms, *Acta Mater.* 188 (2020) 435–474.
- [56] Q. Zhang, R. Huang, X. Zhang, T. Cao, Y. Xue, X. Li, Deformation mechanisms and remarkable strain hardening in single-crystalline high-entropy-alloy micropillars/nanopillars, *Nano Lett.* 21 (8) (2021) 3671–3679, [Online]. Available: <https://www.ncbi.nlm.nih.gov/pmc/articles/33756077/>.
- [57] Z.H. Aitken, Y.-W. Zhang, Revealing the deformation twinning nucleation mechanism of BCC HEAs, *MRS Commun.* 9 (1) (2019) 406–412.
- [58] N. Sakaguchi, M. Niinomi, T. Akahori, J. Takeda, H. Toda, Relationships between tensile deformation behavior and microstructure in Ti–Nb–Ta–Zr system alloys, *Mater. Sci. Eng. C* 25 (3) (2005) 363–369.
- [59] R. Gröger, J. Holzer, T. Kruml, Twinning and antitwinning in body-centered cubic metals, *Comput. Mater. Sci.* 216 (2023).
- [60] H. Tobe, H.Y. Kim, T. Inamura, H. Hosoda, S. Miyazaki, Origin of 332 twinning in metastable β -Ti alloys, *Acta Mater.* 64 (2014) 345–355.
- [61] C.J. Healy, G.J. Ackland, Molecular dynamics simulations of compression–tension asymmetry in plasticity of Fe nanopillars, *Acta Mater.* 70 (2014) 105–112.
- [62] C. Lee, G. Song, M.C. Gao, L. Ouyang, K. An, S.J. Fensin, P.K. Liaw, Effects of Zr addition on lattice strains and electronic structures of NbTaTiV high-entropy alloy, *Mater. Sci. Eng. A* 831 (2022) 142293, [Online]. Available: <https://www.sciencedirect.com/science/article/pii/S0921509321015574>.
- [63] C. Lee, C. Lear, M. Meyers, G. Song, N. Li, Dynamic Deformation Behaviors in Single Body-Centered-Cubic (BCC) phase Refractory High-entropy Alloys.
- [64] F. Maresca, W.A. Curtin, Mechanistic origin of high strength in refractory BCC high entropy alloys up to 1900K, *Acta Mater.* 182 (2020) 235–249.
- [65] C. Lee, F. Maresca, R. Feng, Y. Chou, T. Ungar, M. Widom, K. An, J.D. Poplawsky, Y.-C. Chou, P.K. Liaw, et al., Strength can be controlled by edge dislocations in refractory high-entropy alloys, *Nat. Commun.* 12 (1) (2021) 5474.
- [66] D. Rodney, J. Bonneville, Dislocations, in: *Physical Metallurgy*, Elsevier, 2014, pp. 1591–1680.
- [67] D.R. Trinkle, C. Woodward, The chemistry of deformation: How solutes soften pure metals, *Science* 310 (5754) (2005) 1665–1667.
- [68] Y.-J. Hu, M.R. Fellinger, B.G. Butler, Y. Wang, K.A. Darling, L.J. Kecske, D.R. Trinkle, Z.-K. Liu, Solute-induced solid-solution softening and hardening in bcc tungsten, *Acta Mater.* 141 (2017) 304–316.
- [69] L. Ventelon, F. Willaime, E. Clouet, D. Rodney, Ab initio investigation of the peierls potential of screw dislocations in bcc Fe and W, *Acta Mater.* 61 (11) (2013) 3973–3985.
- [70] M. Itakura, H. Kaburaki, M. Yamaguchi, First-principles study on the mobility of screw dislocations in bcc iron, *Acta Mater.* 60 (9) (2012) 3698–3710.
- [71] J.R. Stephens, Dislocation structures in single-crystal tungsten and tungsten alloys, *Metall. Mater. Trans. B* 1 (1970) 1293–1301.
- [72] J. Shields, R. Gibala, T. Mitchell, Dislocation substructure in Ta-Re-N alloys deformed at 77 K, *Metall. Mater. Trans. A* 7 (1976) 1111–1121.
- [73] E.P. George, W. Curtin, C.C. Tasan, High entropy alloys: A focused review of mechanical properties and deformation mechanisms, *Acta Mater.* 188 (2020) 435–474.
- [74] F. Maresca, W.A. Curtin, Theory of screw dislocation strengthening in random BCC alloys from dilute to “High-Entropy” alloys, *Acta Mater.* 182 (2020) 144–162.